pubs.acs.org/Biomac

Article

EGFR Targeted Redox Sensitive Chitosan Nanoparticles of Cabazitaxel: Dual-Targeted Cancer Therapy, Lung Distribution, and Targeting Studies by Photoacoustic and Optical Imaging

Vikas, Abhishesh Kumar Mehata, Matte Kasi Viswanadh, Ankit Kumar Malik, Aseem Setia, Pooja Kumari, Sanjeev Kumar Mahto, and Madaswamy S. Muthu*

Cite This: https://doi.org/10.1021/acs.biomac.3c00658

Read Online

ACCESS | Metrics & More | Article Recommendations | Supporting Information

ABSTRACT: In this research, we have modified tocopheryl polyethylene glycol succinate (TPGS) to a redox-sensitive material, denoted as TPGS-SH, and employed the same to develop dual-receptor-targeted nanoparticles of chitosan loaded with cabazitaxel (CZT). The physicochemical properties and morphological characteristics of all nanoparticle formulations were assessed. Dual-receptor targeting redox-sensitive nanoparticles of CZT (F-CTX-CZT-CS-SH-NPs) were developed by a combination of pre- and postconjugation techniques by incorporating synthesized chitosan-folate (F) and TPGS-SH during nanoparticle synthesis and further postconjugated with cetuximab (CTX) for epidermal growth factor receptor (EGFR) targeting. The *in vitro* release of the drug was seemingly higher in the redox-sensitive buffer media (GSH, 20 mM) compared to that in physiological buffer. However, the extent of cellular uptake of dual-targeted nanoparticles was significantly higher in A549 cells than other control nanoparticles. The IC_{50} values of F-CTX-CZT-CS-SH-NPs against A549 cells was 0.26 ± 0.12 μg/mL, indicating a 6.3-fold and 60-fold enhancement in cytotoxicity relative to that of dual-receptor targeted, nonredox sensitive nanoparticles and CZT clinical injection, respectively. Furthermore, F-CTX-CZT-CS-SH-NPs demonstrated improved anticancer activity in the benzo(a)pyrene lung cancer model with a higher survival rate. Due to the synergistic combination of enhanced permeability and retention (EPR) effect of small-sized nanoparticles, the innovative and redox sensitive TPGS-SH moiety and the dual folate and EGFR mediated augmented endocytosis have all together significantly enhanced their biodistribution and targeting exclusively to the lung which is evident from their ultrasound/photoacoustic and *in vivo* imaging system (IVIS) studies.

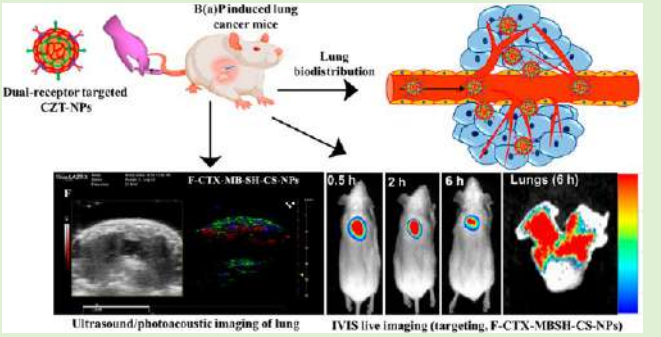

INTRODUCTION

Cancer is the leading cause of mortality worldwide, inflicting over 10 million deaths, or affecting one in every six individuals as per the World Health Organization (WHO) statistics published in 2020. The most frequent cancers are those of the breast, lung, colon, rectum, and prostate.[1] Although standard chemotherapeutic agents are very effective in destroying cancer cells, but they can be devastating to normal cells too, causing severe side effects such as nausea, hair loss, tiredness, etc.[2] Cabazitaxel (CZT) is a semisynthetic derivative of taxane. The Food and Drug Administration (FDA) has approved the use of CZT for metastatic castration-resistant prostate cancer treatment. Besides its notable anticancer properties, CZT has been associated with several significant side effects, including neutropenia, anemia, thrombocytopenia, as well as nausea and vomiting. More precise targeting of these medications to cancer cells necessitates exploration of the cancer cell microenvironment. Cancer cells exhibit certain characteristics, including the overexpression of specific receptors and a heightened redox potential. These characteristics can be utilized in the development of drug delivery systems that have potential applications in cancer therapy. This high redox potential is due to the increased production of reactive oxygen species (ROS) by cancer cells and their elevated glycolytic activity.[3] Cancer cells produce more glutathione (GSH, a tripeptide containing cysteine) to protect themselves from oxidative stress, and its high concentration can mitigate the oxidation of the sulfhydryl (SH) group, making them more susceptible to cleavage.[4] Various reports suggested that thiolated polymer-based nanomedicine improves drug delivery by enhancing the bioadhesion property, delaying lysosomal degradation, and increasing drug release in the cells after

Received: July 4, 2023
Revised: September 25, 2023

endocytosis.[5] However, the exact mechanism of this has yet to be well understood. The level of GSH in cancer cells (20 mM) is much higher than that of the blood circulation (2−20 μM). After internalization in the cancer cells, the SH group of thiolated nanomedicine forms a dithiol intermediate with GSH, which is then oxidized and triggers the instant release of the drug.[6,7] Recently, 4-aminothiophenol conjugated D-alpha-tocopheryl polyethylene glycol 1000 succinate (TPGS-SH), a modification of TPGS using 4-amino thiophenol, has been employed in the development of redox-sensitive nanomedicine for enhanced cancer therapy.[8] In addition to the aforementioned alterations, it is worth noting that TPGS is an excipient that has received approval from the FDA. Additionally, it improves the properties of cancer nanomedicine by acting as a P-glycoprotein inhibitor and through the process of PEGylation, it also confers stealth properties to the nanomedicines.[9] Moreover, numerous thiolated nanomedicines have been developed that have improved anticancer effects, such as mesoporous silica nanoparticles (NPs),[10] β-cyclodextrin modified iron oxide NPs,[11] chitosan NPs,[12] gold NPs,[13] and chitosan-modified TPGS copolymer NPs.[14] However, our previous research has demonstrated that folate- and EGFR (dual)-targeted NPs of CZT are particularly successful in targeting specifically to cancer sites.[15] Furthermore, the efficiency of dual-receptor targeted NPs can be enhanced by adopting redox-sensitive properties.

Cigarette smoke and tobacco consumption are the key reasons for the development of various cancers, including lung, mouth, and throat cancer. Cigarette smoke contains a variety of carcinogens, but benzo[a]pyrene (B(a)P) is the most prevalent and its carcinogenic properties are well documented.[16] The present study sought to demonstrate that redox-sensitive NPs with dual receptor targeting could treat lung cancer caused by cigarette smoke by inducing lung cancer in mice with the B(a)P and evaluating the anticancer ability of the formulations. Since folate and EGF receptors are highly expressed in the majority of cancers, they can be exploited to develop dual-receptor targeted nanomedicine. Cetuximab (CTX) is a chimeric monoclonal antibody that exclusively targets and binds to the EGFR. The U.S. FDA authorized it in 2014. It has been employed to develop EGFR-targeted nanosystems including iron-oxide NPs,[5] PLGA-NPs,[17] PLGA-ZnS-NPs,[18] silica NPs,[19] and chitosan NPs. Moreover, folic acid has been approved by the FDA for megaloblastic anemias and also has been used as a potential ligand for the folate receptor based targeted delivery of various anticancer medications[15,20] and therefore was selected for the present investigation. Chitosan (CS) is a commonly employed natural polymer due to its remarkable mucoadhesion, biocompatibility, biodegradability, and nontoxic properties.[21] Consequently, it has been chosen as the polymer for the development of the proposed redox-sensitive nanomedicine. However, due to the lipophilic nature of the CZT, various fluorescent materials with similar physicochemical properties have been chosen for specific characterization so that they can be used with the same loading procedure used for the CZT, such as coumarin-6 for cellular uptake,[22] methylene blue as a contrast agent for photoacoustic,[23] and DiD dye for IVIS.[24]

In this study, we have developed dual-receptor targeted, TPGS-SH-based CZT chitosan NPs and analyzed in depth their anticancer activity and evaluated their lung biodistribution using ultrasound/photoacoustic imaging and dual targeting efficiency by IVIS live imaging in a B(a)P induced lung cancer in mice model.

MATERIALS AND METHODS

Cabazitaxel (CZT) was a gift sample, provided by Dr. Reddy's Laboratories, Hyderabad, India. 4-Aminothiophenol (4-ATP), 1-ethyl-3-(3-(dimethylamino)propyl) carbodiimide (EDC), folic acid, benzopyrene, Cetuximab (CTX), methylene blue (MB), *N*-hydroxy succinimide (NHS), DMAP (4-dimethylaminopyridine), and coumarin-6 (C6) were supplied by Sigma-Aldrich, USA. Chitosan (deacetylation degree ≤ 90% and MW ∼ 1500 Da) and succinic anhydride were obtained from Sisco Research Laboratory Pvt. Ltd. (SRL) India. Antares Health Products, Inc. gifted TPGS (D-alpha-tocopheryl-polyethylene glycol-1000-succinate). A 1 kDa dialysis membrane (Sigma-Aldrich) was procured from Spectrum Laboratories-Bioz, USA. TEM grids (carbon coated, 400 mesh size) were obtained from Sree analytical Inc., Hyderabad, India. A549 (human adenocarcinoma) and SIRC (Statens seruminstitut rabbit cornea) cell lines were obtained from the National Centre for Cell Science (NCCS) in Pune, India. MTT was supplied by Biotium, USA. Dulbecco's modified Eagle's medium (DMEM), fetal bovine serum, PBS-10X, 4′,6-diamidino-2-phenylindole (DAPI), paraformaldehyde solution (4%), and antibiotics solution 100X liquid were all provided by HIMEDIA laboratories. 1,1′-Dioctadecyl-3,3,3′,3′-tetramethylindodicarbocyanine, 4-chlorobenzenesulfonate salt (DiD dye) was purchased from Thermo Fisher Scientific, India. All of the other chemicals and reagents utilized in the investigation were of analytical grade.

Nomenclature of Nanoparticles. Nanoparticles are assigned distinct nomenclatures that follow a specific order, starting from the right side, to convey information effectively. This sequence includes NPs (nanoparticles), SH (redox sensitive), CS (chitosan polymer), CZT (cabazitaxel loading), CTX (cetuximab targeting ligand for EGFR), and F (folate targeting). The combination of these acronyms can be used to determine which nanoparticles are being discussed.

Preparation of Cross-Linked Chitosan-Folate (CS-F). The CS-F was prepared and characterized by a method reported previously that involves the reaction of the folic acid with CS using a carbodiimide cross-linker (EDC).[25] The extent of folate conjugation to CS was estimated by the method reported previously.[26] Moreover, the physical state of chitosan and prepared CS-F was analyzed by X-ray diffraction (XRD).

Synthesis of Thiolated TPGS (TPGS-SH). The synthesis of TPGS-SH was accomplished in two steps as demonstrated in Figure S1. The first step involves the functionalization of TPGS with the terminal free carboxyl group (referred as to as TPGS-COOH) by ring opening reaction with succinic anhydride in the presence of DMAP at 100 °C for 24 h in a N_2 atmosphere. All of the reaction conditions were maintained as reported previously.[27] Briefly, 161.4 mg of TPGS-COOH (0.1 M) and 31 mg of EDC (0.2 M) were dissolved in 10 mL of absolute ethanol and stirred for the next 1 h in darkness. Then, 25 mg of 4-aminothiophenol (4-ATP; 0.2 M) was added to the above solution and allowed to stir for the next 24 h. The reaction mixture was further dialyzed with a 1KD dialysis membrane in distilled water to remove unreacted reagents and stored at 4 °C after lyophilization for 24 h.[28]

Characterization of TPGS-SH. FTIR, NMR, and mass spectroscopy were used to characterize the synthesized TPGS-SH. The thiol group content in TPGS-SH was determined by UV spectrometry using Ellman's assay.[7] The reaction between Ellman's reagent and thiols gives a yellow-colored dianion of 2-nitro-5-thiobenzoic acid (NTB^{2-}) and a disulfide, which can be detected at a lambda max of 420 nm. Briefly, stock solutions of 4-ATP were prepared in ethanol, and 80 μL of each of them was incubated with 160 μL of Ellman's reagent in 96-well plates. The percentage of thiol groups was determined by the calibration curve of 4-ATP. Moreover, the physical states of TPGS, TPSH−COOH, and TPGS-SH were revealed by the XRD analysis.

https://doi.org/10.1021/acs.biomac.3c00658
Biomacromolecules XXXX, XXX, XXX−XXX

Formulation of CZT/Coumarin 6 (C6)/Methylene Blue (MB)/DiD Dye Loaded CS-NPs. The earlier established method was employed to prepare the CZT-CS-NPs, CZT-CS-SH-NPs, F-CZT-CS-SH-NPs, CXT-CZT-CS-SH-NPs, and F-CXT-CZT-CS-SH-NPs with slight alterations. All of the necessary ingredients were taken as mentioned in Table S3. CS and CS-F were solubilized in 1% aqueous acetic acid solution, and the pH was adjusted to 6.0 using NaOH solution. Then, 1 mL of 20 mg/mL of TPGS or TPGS-COOH and TPGS-SH aqueous solution was added to the CS phase. Following this, 1 mL of a CZT solution in chloroform was added, and the resulting two-phase system was sonicated for 5 min. The prepared emulsion was then swirled overnight to ensure the complete removal of chloroform. Then, 2.5 mL of sodium tripolyphosphate (Na-TPP) solution (2 mg/mL) was added dropwise and stirred for 1 h. To remove larger particles, the NPs dispersion was centrifuged at 1000 rpm for 5 min, and the supernatant was separated and passed through a 0.22 μm membrane filter. To prepare the F-CZT-CS-SH-NPs, the required quantities of CS-F, together with CS, were employed. Furthermore, TPGS-COOH was also added, in addition, to the preparation of CTX-CZT-CS-SH-NPs. The resulted carboxylated CS-NPs were then agitated for 30 min with EDC/NHS (1:5 molar ratio respective to TPGS-COOH). The aforementioned NPs dispersion was then mixed with 2.5 mg of CTX for 30 min and then dialyzed in saturated CZT solution for 30 min to remove the unreacted cross-linker and CTX. Moreover, for the preparation of F-CTX-CZT-CS-SH-NPs, CS-F and TPGS-COOH were added, followed by the addition of the CTX, while the remaining steps were similar.

Further, a batch of C6-loaded CS-NPs (C6-CS-NPs, C6-CS-SH-NPs, F-C6-CS-SH-NPs, CTX-C6-CS-SH-NPs, and F-CTX-C6-CS-SH-NPs) was developed for the cellular-uptake experiment by loading C6 rather than CZT. Similarly, a set of all CS-NPs (MB-CS-NPs, MB-CS-SH-NPs, F-MB-CS-SH-NPs, CTX-MB-CS-SH-NPs, and F-CTX-MB-CS-SH-NPs) were prepared for photoacoustic imaging by incorporating 50 μg of MB dye instead of CZT. Finally, for IVIS fluorescence imaging, instead of CZT, 2 μg of DiD dye was used for the preparation of DiD dye loaded CS-NPs (DiD-CS-NPs, DiD-CS-SH-NPs, F-DiD-CS-SH-NPs, CTX-DiD-CS-SH-NPs, and F-CTX-DiD-CS-SH-NPs) with the same technique.

Nanoparticles Characterization. The methods employed for the characterization of nanoparticles, such as particle size, shape, and morphology (transmission electron microscopy and atomic force microscopy); surface chemistry; degree of conjugation; XRD; and entrapment efficiency, are detailed in the Supporting Information (S1 to S7).

***In-Vitro* Characterization.** *In Vitro Release Study.* The percent CZT released from the various CS-NPs in GSH buffer solutions (5 mM and 20 mM) was analyzed by the dialysis bag diffusion method at pH 7.4 and pH 5.5.[29] A volume of CS-NPs containing 0.3 mg of the drug was introduced in a dialysis bag and sealed with plastic closures. This setup was positioned in a beaker having 50 mL of buffer while swirling continuously in a shaking water bath apparatus (REMI CM-12 PLUS) at 37 ± 0.5 °C. At the prescheduled time intervals, 1 mL of the media was collected and passed through a membrane filter, while fresh media was added to maintain the constant volume of the media in the flask. The CZT concentration was determined by HPLC analysis. The percent cumulative drug release versus time graph was plotted. Further, the time at which 50% of the drug was released (T_{50}) was computed for a comparative assessment of the drug release from the NPs.

In-Vitro Cellular Uptake Analysis. To assess the targetability of the dual-receptor targeted NPs of CZT, a comparative cellular uptake analysis of C6-loaded NPs was performed in A549 cancer cells. Cells, at a density of 5×10^4 cells per well, were seeded in a 12-well plate and allowed to grow for 24 h. Thereafter, the NPs were incubated for 12 h with a 5 μg/mL concentration of C6. For the fixation, the cells were treated with 4% formaldehyde for 15 min. To stain the nucleus blue, DAPI was added. After 15 min, the media were withdrawn, and the cells were washed with PBS. The images were acquired in a fluorescent microscope (Nikon, Ti−U, EINST Technology Pte Ltd.) with blue (DAPI) and green (C6) fluorescence filters, and the intensity of green fluorescence that shows the extent of particle internalization was assessed by the Image-J software.[27]

MTT Assay. The MTT assay was carried out to determine the effect of dual-receptor targeted SH-NPs on A549 (human adenocarcinoma) and SIRC (Statens seruminstitut rabbit cornea) cells. The cytotoxicity of SH-NPs was compared with their nonthiolated equivalent NPs. In a 96-well culture plate, the cells were seeded at a density of 5×10^4 cells per well in DMEM and placed in a CO_2 humidified incubator for 24 h. Then, the cells were treated with corresponding CS-NPs at concentrations from 25 μg/mL to 0.025 μg/mL made by serial dilution in the DMEM medium. After removing the depleted media, the cells were treated with 10 μL of 5 mg/mL solution of MTT in PBS, at pH 7.4, with 90 μL of fresh DMEM, and incubated for 2 h. The medium was then removed while keeping the formazan crystals undisturbed. Crystals were washed with PBS and dried for 2 h. Further, 0.1 mL of DMSO was transferred, and the culture plate was shaken. The absorbance of the samples was recorded at a wavelength of 570 nm with the help of a multimode-microplate reader.[30] The cell viability (%) was determined by employing the formula below.

$$\%\text{Cellular viability} = \frac{\text{Absorbance of treated samples}}{\text{Absorbance of negative control}} \times 100$$

Morphological Analysis. The cytotoxicity of developed CS-NPs was further examined by comparing their effects on the cell nucleus and cytoskeleton, which were labeled with DAPI and F actin-staining (phalloidin-tetramethylrhodamine conjugate), respectively. In a 12-well plate, A549 cells were plated in wells with 5×10^3 cells per well and allowed to grow for 24 h. Following this, the cells were treated for 12 h with CS-NPs at a concentration corresponding to the IC_{50} value of the F-CTX-CZT-CS-SH-NPs. After removing the treated medium, the cells were rinsed three times with PBS. Before staining with DAPI, the cells were fixed for 20 min in a 4% formaldehyde solution. The cells were rinsed in PBS and treated for 5 min with triton-X 100. Subsequently, the cells were treated with an F-actin staining agent for 30 min and studied for morphological changes under a fluorescent microscope (Nikon, Ti−U, EINST Technology Pte Ltd.).[31]

In Vivo Evaluation. *Ethics Statement.* Animals experiments in this study were approved by the Institutional Animal Ethics Committee (IAEC), Department of Pharmaceutical Engineering and Technology, Indian Institute of Technology (BHU) Varanasi (IAEC Approval Number: IIT(BHU)/IAEC/2022/046). The *in vivo* experiments were carried out as per the guidelines of the IAEC at the IIT (BHU), Varanasi. All animal experiments comply with the National Research Council's Guide for the Care and Use of Laboratory Animals.

Induction of Lung Cancer in Mice. In the study, Swiss albino mice weighing 15−20 g were employed. Animals were provided with controlled humidity and temperature facilities. B(a)P at a dose of 50 mg/kg orally was used for lung cancer induction. The required quantity of the carcinogen was dispersed in corn oil. The control group received a comparable volume of blank corn oil. The B(a)P dispersion was given twice a week for 4 weeks. However, an additional cancer model group was used to check the initiation of cancer induction on the 14th day of B(a)P exposure.[32]

Lung Biodistribution by Ultrasound/Photoacoustic Imaging. A multimodal *in vivo* imaging system was used to compare the extent of biodistribution of dual-targeted MB loaded CS-SH-NPs with MB control and other MB-loaded NPs in a B(a)P-induced lung cancer mice model. The experiment employed Swiss albino mice (n = 3, males), weighing 16−20 g that were maintained in controlled temperature and humidity conditions with continual humidity-free access to water and fed with a standard rodent diet. The mice were divided into seven groups and injected with MB control and MB-CS-NPs, MB-CS-SH-NPs, F-MB-CS-SH-NPs, CTX-MB-CS-SH-NPs, and F-CTX-MB-CS-SH-NPs. Furthermore, F-CTX-MB-CS-SH-NPs were also injected into healthy mice to compare their biodistribution with the cancer model. The animals were anaesthetized during the experiment by inhalational isoflurane (3% for induction and 1.5−2% for maintenance) at 1.2 L/min of oxygen flow. Afterward, the animals

https://doi.org/10.1021/acs.biomac.3c00658
Biomacromolecules XXXX, XXX, XXX−XXX

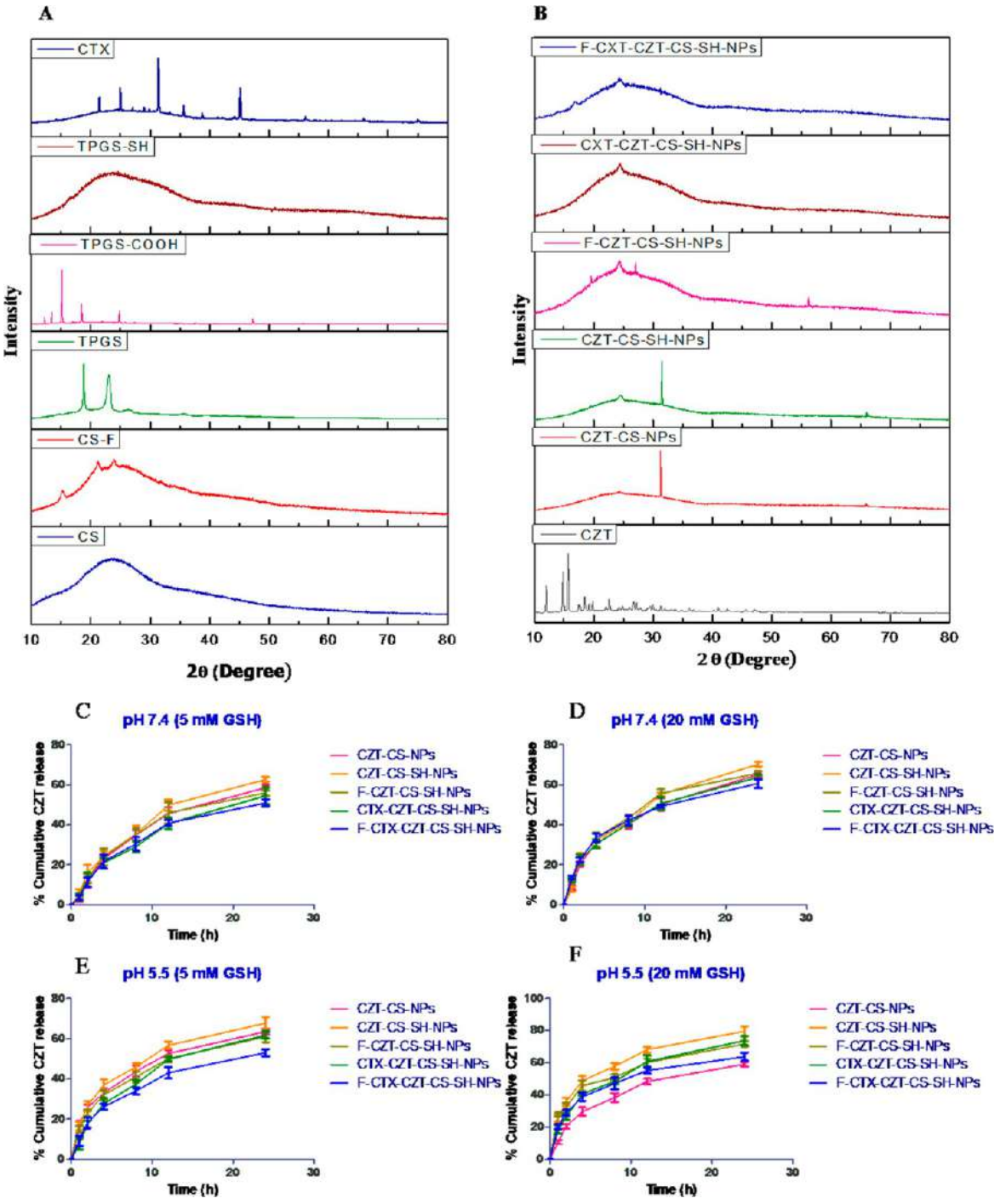

Figure 1. XRD pattern of (A) CS, CS-F, TPGS, TPGS-COOH, TPGS-SH, and CTX. (B) CZT and CZT loaded CS-NPs. (C) *In vitro* CZT release profile of CS-NPs at (C) pH 7.4 (5 mM GSH), (D) pH 7.4 (20 mM GSH), (E) pH 5.5 (5 mM GSH), (F) pH 5.5 (20 mM GSH).

were placed in a supine posture on a heated working table (Fujifilm VisualSonics, Inc.). An ultrasonic transducer with a jacket containing a small (14 mm) optical fiber bundle (Fujifilm VisualSonics, Inc.) was positioned above the animal to provide the best parasternal long-axis image of the lungs. A bubble-free clear ultrasonic gel (OXD, Spain) was used to cover the 5 mm gap between the transducer surface and the animal skin. Throughout all scans, the total image depth was set at 18 mm. The PA signal was collected before and after 30 min of intravenous administration of MB control and MB loaded NPs through the tail vein.

The acquired data were processed using VevoLAB software V.3.2.5 (Fujifilm VisualSonics, Inc.). To reduce the natural PA signal arising from hemoglobin, an initial value of the PA signal obtained before the NPs delivery was removed in all scans using a Subtraction Control tool. The animal studies were carried out in accordance with CPCSEA regulations.[33]

Targeting Efficiency to Lungs by IVIS Live Imaging. *In vivo* fluorescence imaging of DiD control and DiD-loaded CS NPs was performed on B(a)P induced lung cancer mice using the Photon Imager Optima System (Biospace Lab). The CS-NPs, equivalent to 200 nM of DiD dye, were administered intravenously by tail vein, and the fluorescence signals were captured at excitation and emission wavelengths of 620 and 710 nm respectively at 0.5, 2, and 6 h postinjection. The radiant efficiency (measured as fluorescence intensity/area/time) was analyzed using the Biospace Lab imaging software by region of interest (ROI) tool, circling the lung area.[34]

https://doi.org/10.1021/acs.biomac.3c00658
Biomacromolecules XXXX, XXX, XXX−XXX

Table 1. Particle Size, Polydispersity Index, Zeta Potential, Entrapment Efficiency, and IC_{50} Values[a]

formulations	PS (nm) (mean ± SD*)	PDI (mean ± SD*)	ZP (mV) (mean ± SD*)	EE (%) (mean ± SD*)	IC_{50} value (A549 cells; mean ± SD*)
CZT (control)					15.7 ± 2.3
CZT-CS-NPs	115.0 ± 4.26	0.181 ± 0.07	+28.4 ± 3.7	79.4 ± 4.2	9.6 ± 1.5
CZT-CS-SH-NPs	120.5 ± 6.20	0.162 ± 0.03	+26.5 ± 2.8	78.8 ± 3.0	6.4 ± 0.8
F-CZT-CS-SH-NPs	127.1 ± 4.25	0.194 ± 0.04	+23.8 ± 3.6	72.5 ± 3.5	2.8 ± 0.6
CTX-CZT-CS-SH-NPs	135.5 ± 3.30	0.310 ± 0.06	+19.2 ± 3.4	69.5 ± 3.1	1.5 ± 0.3
F-CTX-CZT-CS-SH-NPs	136.0 ± 4.47	0.333 ± 0.03	+15.5 ± 2.4	67.8 ± 2.5	0.2 ± 0.1
C6-CS-NPs	120.4 ± 3.21	0.231 ± 0.05	+29.8 ± 4.3	72.3 ± 3.4	
C6-CS-SH-NPs	125.0 ± 2.33	0.230 ± 0.03	+27.3 ± 3.3	71.8 ± 2.4	
F-SH-CS-SH-NPs	130.7 ± 4.21	0.276 ± 0.05	+22.6 ± 2.5	68.5 ± 4.0	
CTX-C6-CS-SH-NPs	136.5 ± 2.58	0.279 ± 0.08	+22.3 ± 3.8	66.7 ± 2.4	
F-CTX-C6-CS-SH-NPs	138.5 ± 3.25	0.330 ± 0.09	+20.5 ± 3.5	65.82 ± 4.4	

[a]CZT-CS-NPs: CZT loaded chitosan NPs. CZT-CS-SH-NPs: CZT loaded redox-sensitive chitosan NPs. F-CZT-CS-SH-NPs: CZT loaded folic acid conjugated redox-sensitive chitosan NPs. CTX-CZT-CS-SH-NPs: CZT loaded cetuximab conjugated redox-sensitive chitosan NPs. F-CTX-CZT-CS-SH-NPs: CZT loaded cetuximab and folic acid conjugated redox-sensitive chitosan NPs. C6-CS-NPs: C6 loaded chitosan NPs. C6-CS-SH-NPs: C6 loaded redox-sensitive chitosan NPs. F-C6-CS-SH-NPs: C6 loaded folic acid conjugated redox-sensitive chitosan NPs. CTX- C6-CS-SH-NPs: C6 loaded cetuximab conjugated redox-sensitive chitosan NPs. F-CTX-C6-CS-SH-NPs: C6 loaded cetuximab and folic acid conjugated redox-sensitive chitosan NPs. PS, particle size; PDI, polydispersity index; ZP, zeta potential; EE, entrapment efficiency.

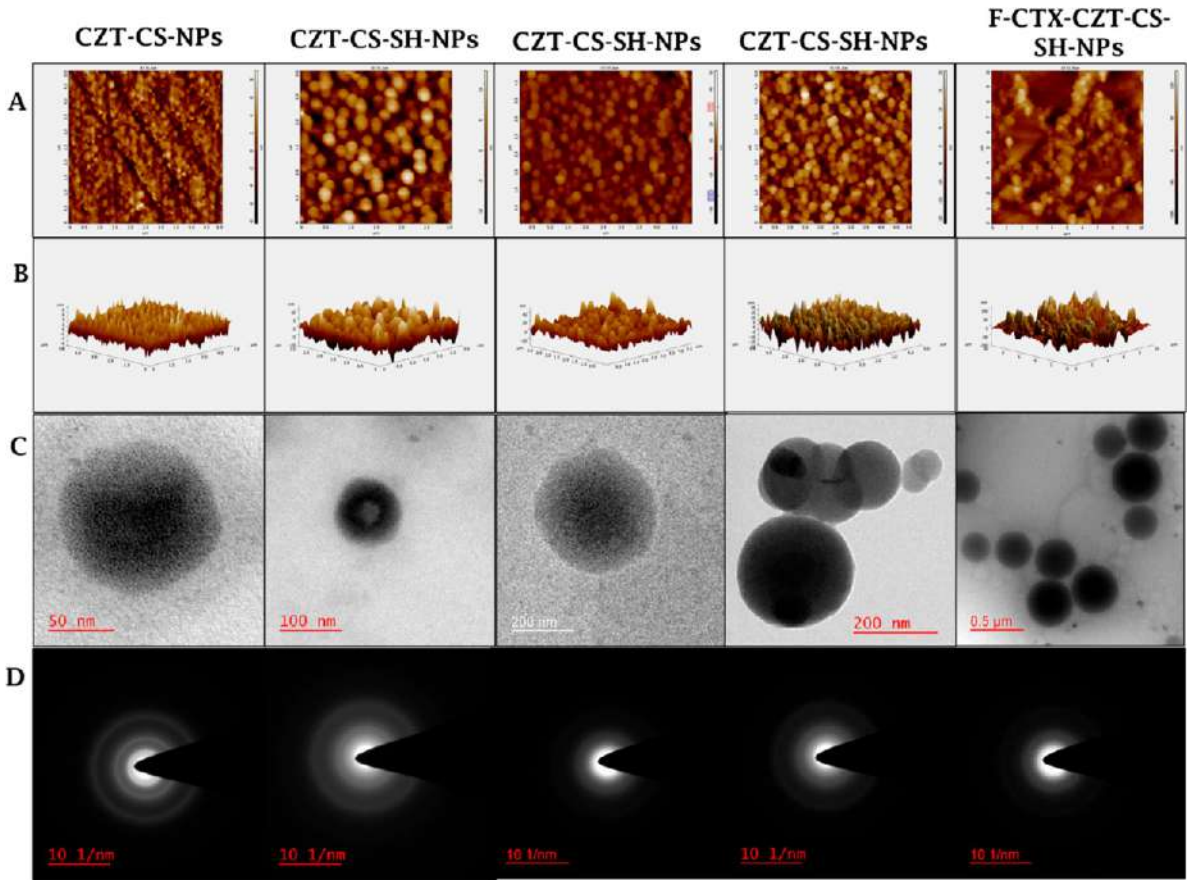

Figure 2. Morphological assessment of CS-NPs by (A) 2D and (B) 3D AFM images, (C) TEM images, and (D) SAED images.

Survival Analysis and Anticancer Efficacy. The animals were randomized into nine groups (n = 5) for the negative control, cancer model, and six treatment groups (with CZT control and other CZT-loaded CS-NPs). The treatments were started intravenously from the 14th day of B(a)P exposure at a dose of 6.5 mg/kg of CZT, twice a week through the tail vein. The lungs of the animals were extracted on the day of death; otherwise, they were euthanized after 120 days for histopathological analysis. The lungs were sliced by a microtome after placement in the paraffin. The slides were prepared after staining with hematoxylin and eosin (HE) dyes. Afterward, the images were captured at a resolution of 10× using a brightfield microscope. The violet channels in the image represent the nucleus, as they are stained violet by hematoxylin dye. ImageJ software was used to separate the violet channels, employing the "split channels" tool to assess the area of the nuclei. To analyze the nuclei area, the images were again processed into a binary image (black and white). To calculate the percent survival rate, the Kaplan−Meier survival analysis was performed.[35]

https://doi.org/10.1021/acs.biomac.3c00658
Biomacromolecules XXXX, XXX, XXX−XXX

Histopathology Study. The histopathological study was performed on Wistar rats to assess the safety of prepared NPs in comparison to CZT control. Seven animal groups, with four rats in each, were used in this experiment. The control group received saline; the remaining animal groups were given CZT control and five CS-NPs formulations at a dose of 3.5 mg per kilogram of the body weight of the drug. Formulations were administered intravenously thrice at an interval of 3 days, and rats were sacrificed after 2 weeks. The sections of the vital organs, including the lungs, liver, kidneys, and heart, were prepared and processed with HE staining as the method reported.[36] The histopathological alterations were seen using a light microscope (Olympus, India), and images were acquired using the Top View 3.7 software.

Statistical Analysis. All the statistical analyses were performed by using one-way ANOVA for calculating statistical differences among the groups. The significance level is denoted by ns ($p \geq 0.05$), * ($p < 0.05$), ** ($p < 0.01$), and *** ($p < 0.001$).

RESULTS AND DISCUSSION

Evaluation of CS-F. In order, to prepare the folic acid conjugated NPs, the CS-F was prepared and characterized by FTIR and NMR, as reported previously.[37]

Degree of Substitution. The degree of folic acid substituted to the CS was 0.71 ± 0.06. This indicates that about 71% of the folic acid was substituted to CS, which indeed aligns with the previous findings.[38]

XRD Analysis. XRD analysis was used to assess the physical state of the synthesized CS-F. The XRD spectra of CS exhibited broad peaks revealing its amorphous state, whereas, in the XRD spectra of CS-F, extra sharp peaks were observed between 2θ = 15 and 25°demonstrating its semiamorphous nature, which supported the conjugation of CS with folic acid (Figure 1A). Naglah et al. also examined the crystalline properties of folic acid and its impact on the physical state of the modified compound using XRD, which is consistent with our observations.[39] Moreover, the XRD spectra of pure CTX showed its crystalline nature, but these peaks were missed in the CTX targeted NPs, stating its change in state after conjugation with the NPs, which might be dominated with the amorphous characteristics of CS.

Evaluation of TPGS-SH. *FTIR Spectroscopy.* The FTIR spectra of TPGS, TPGS-COOH, and TPGS-SH were compared to analyze the synthesized TPGS-SH, as shown in Figure S2. The N−H stretching and bending vibrations were detected in the TPGS-SH spectra at 3350 cm^{-1} and 1629 cm^{-1}, respectively, whereas the stretching vibration of C═O, C−O−C, C−O, and aromatic C−H was observed at 1703 cm^{-1}, 1051 cm^{-1}, 1223 cm^{-1}, and 1497 cm^{-1}, respectively. However, a broad peak of OH stretching was identified in the TPGS spectral graph and TPSG-COOH at 3448 and 3500 cm^{-1}, respectively. Table S1 in the Supporting Information showed all the characteristic peaks related to their functional groups.

^{1}H NMR Spectroscopy. ^{1}H NMR and ^{13}C NMR analyses of TPGS-COOH and TPGS-SH were evaluated to confirm the synthesis. The ^{1}H NMR spectra of TPGS-COOH was characterized by identifying different ethylene groups, which were also present in TPGS-SH spectra with slight changes. The methylene protons of the 1,4 diketone segment were observed at 2.69 and 2.89 ppm. In comparison, the methylene protons of polyethylene glycol units $[(CH_2CH_2O)_n]$ were identified at 3.51 and 4.1 ppm. Moreover, the presence of methylene protons of the conjugated succinic anhydride group was identified at 2.37 and 2.98 ppm. Furthermore, the ^{1}H NMR spectra of TPGS-SH consist of several characteristic peaks of distinct functional groups, including the sulfhydryl (SH) and aromatic groups related to 4-ATP. Furthermore, the TPGS-SH spectra also showed the new doublets at 6.5 and 7.0 ppm, associated with the para-disubstituted aromatic ring of conjugated 4-aminothiophenol, whereas these peaks were absent in the spectra of TPGS-COOH. These findings also align with the previous reports.[28] In addition, the ^{13}C NMR spectra of the TPGS-SH also displayed the peak of carbons in the aromatic ring in TPGS-SH at 114.3 and 134.2 ppm, which

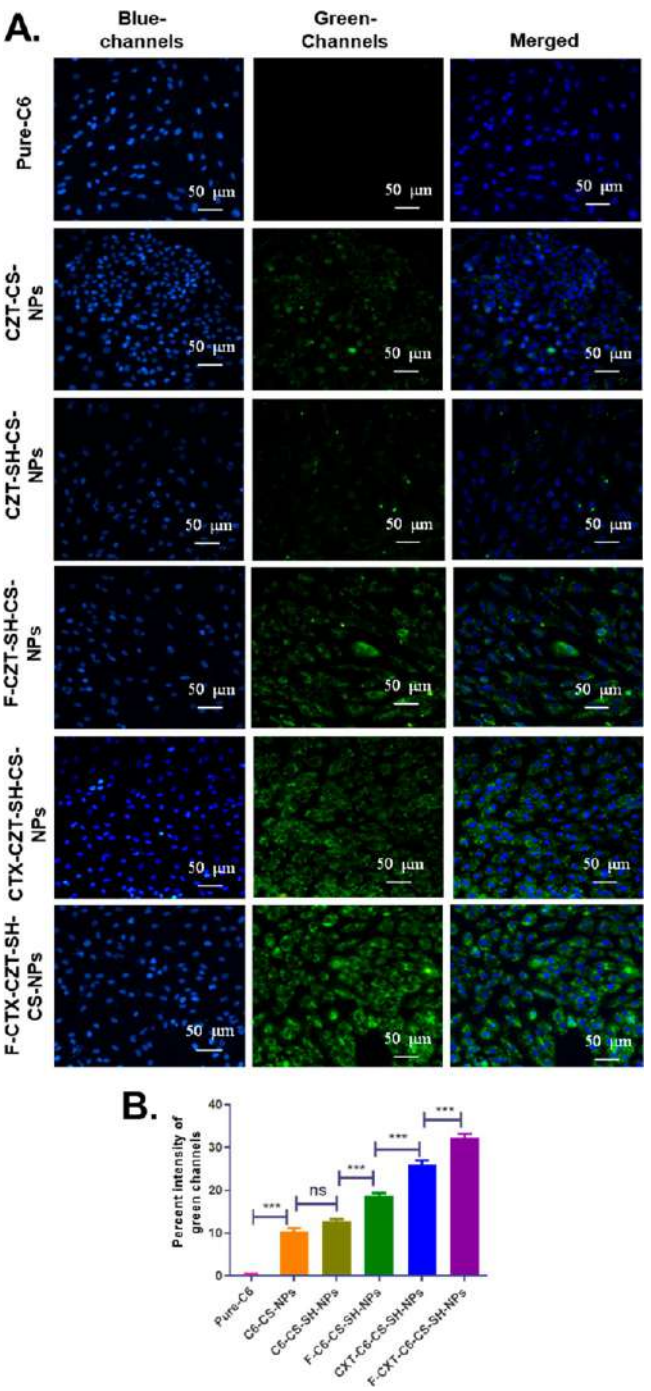

Figure 3. (A) Cellular uptake study, images of A549 cells after 12 h of treatment with pure C6 and C6 loaded CS-NPs and (B) histogram showing the intensity of green fluorescence (%) in A549 cells with pure C6 and C6 loaded CS-NPs after 12 h of incubation.

https://doi.org/10.1021/acs.biomac.3c00658
Biomacromolecules XXXX, XXX, XXX−XXX

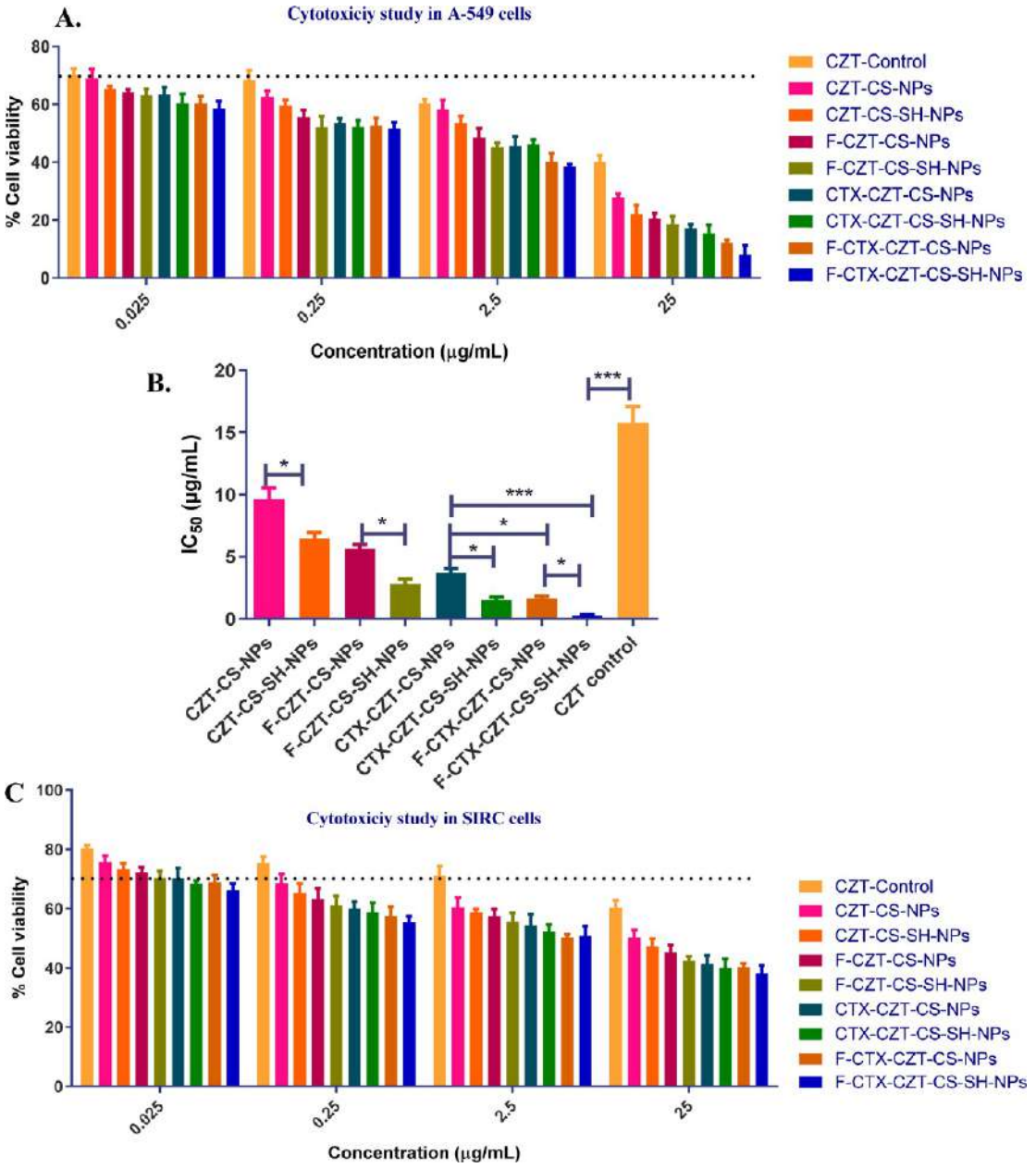

Figure 4. (A) Percent cell viability of of A549 cells after treatment with CS-NPs and CZT control. (B) Histogram showing the IC_{50} value in A549 cells and (C) percent cell viability of SIRC (noncancerous) cells after 24 h of treatment with NPs and CZT control. The dotted lines represent the biocompatibility limits at 70% cell viability.

were absent in TPGS-COOH spectra (Figures S3 and S4). All these findings support the successful synthesis of TPGS-SH.

High-Resolution Mass Spectrometry (HRMS). Supplementary Figure S5 depicts the HRMS spectra of TPGS, TPGS-COOH, and TPGS-SH. Most of the fragmentation peaks observed in the mass spectra of TPGS, TPGS-COOH, and TPGS-SH were repeated after the interval of 22 units and 44 units, demonstrating the presence of the doubly charged species (appears at half mass) and singly charged species, respectively. These peaks were identified for the polyethylene glycol (PEG) units ($-OCH_2CH_2-$, m/z = 44) of the TPGS. The phenomenon of doubly charged species is typical for PEG containing compounds (molecular weight <5 kDa).[40,41,42] Since, TPGS-COOH was prepared by esterification reaction with succinic anhydride (M.W. = 101), the HRMS spectrum of TPGS-COOH consisted of the fragmentation peaks higher at the m/z = 101 units with the comparable peaks in HRMS spectrum of TPGS.[37] The confirmation of TPGS-COOH synthesis by HRMS also stands in agreement with the results reported in previous studies. Since 4-aminothiophenol (M.W. = 125) was employed in the synthesis, the HRMS spectra of TPGS-SH showed respective peaks higher at the m/z = 107 units (125 − 18, as a molecule of water, released), than the HRMS spectra of TPGS-COOH. The fragmentation peaks observed in the TPGS-COOH HRMS graph at m/z 914.1, 957.6, 971.6 1002.2, 1015.7, 1046.7, and 1157.7 and their relative peaks (plus 107 units) were observed in the TPGS-SH HRMS graph at m/z = 1021.5, 1065.5, 1077.5, 1108.2, 1121.5, 1165.5, and 1253.5, respectively. These findings support the synthesis of TPGS-SH. The commercially available TPGS employed as the precursor in this synthesis has a molecular weight of 1513 Da. After comparing the fragmentation pattern

https://doi.org/10.1021/acs.biomac.3c00658
Biomacromolecules XXXX, XXX, XXX−XXX

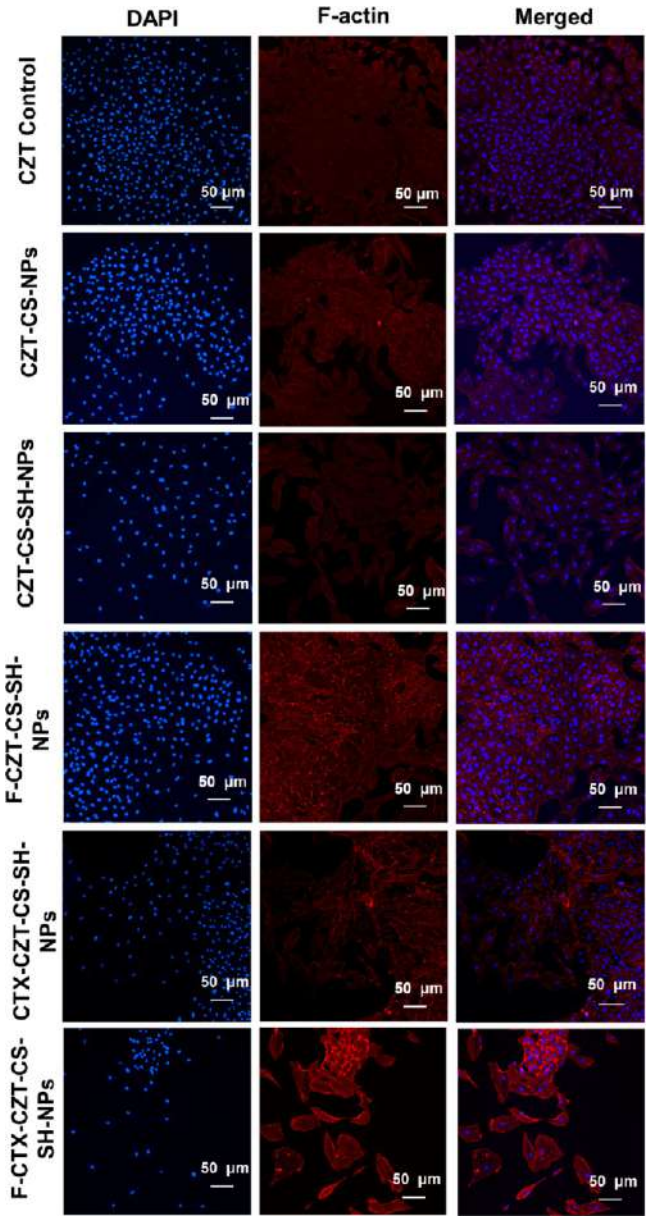

Figure 5. Apoptosis assessment in A549 cells with CZT control and CZT loaded CS-NPs after 12 h of incubation.

associated with the attached function group, it can be inferred that the molecular weight of TPGS-COOH is approximately 1614 Da (101 units higher than TPGS). Additionally, the molecular weight of TPGS-SH is estimated to be 1721 Da, which is 107 units higher than TPGS-COOH.

XRD Spectroscopy. XRD spectroscopy was used to assess the change in the physical state of synthesized TPGS-SH and TPGS-COOH by observing changes in their diffraction patterns compared to the TPGS (Figure 1A). The XRD spectra of TPGS exhibited sharp peaks between a 2θ of 12° and 25°, indicating its crystalline nature. In addition, the XRD spectra of TPGS-COOH exhibited broad peaks demonstrating that it is an amorphous material. Finally, the XRD spectra of TPGS-SH also showed sharp crystalline peaks between a 2θ of 20° and 45°, indicating its crystalline nature.

Particle Size and Zeta Potential Analyses. Table 1 shows the physicochemical characteristics of CZT/C6 loaded CS-NPs. Since the particle size of all of the NPs was less than 200 nm, these can be capable to produce the EPR effect, if administered intravenously in cancer patients. The polydispersity index ranged from 0.1 to 0.3, demonstrating that CS-NPs are highly monodispersed to moderately polydispersed, which is also suitable for the EPR effect and receptor-mediated endocytosis.[43] Moreover, the surface charge of all CS-NPs (+15 to +30 mV) indicates good hydrodynamic stability, as the particles are less likely to aggregate.

AFM. The AFM images of all types of CS-NPs revealed smooth and spherical surfaces without visible pinholes (Figure 2A,B).

Transmission Electron Microscopy (TEM) Analysis. The TEM images of all CS-NPs demonstrated their spherical shape, and the particle size data from TEM images are in absolute tune with that obtained from DLS measurements (Figure 2C). Further, the selected area electron diffraction (SAED) images of CZT-CS-NPs displayed concentric circles, demonstrating their polycrystalline nature. However, the SAED images of CZT-CS-SH-NPs and F-CTX-CZT-CS-SH-NPs exhibited diffused rings, indicating their amorphous state (Figure 2D).

Surface Chemistry. The X-ray photoelectron spectroscopy (XPS) survey of each CS-NPs, consisting of various peaks of nitrogen (N 1s), carbon (C 1s), oxygen (O 1s), and sulfur (S 2p), ranged in binding energies at 408−390 eV, 298−280 eV, 545−529 eV, and 162−165 eV, respectively (Figure S6A). The atomic percentage of N 1s and S 2p in the XPS spectra is shown in Figure S6B. The atomic percentage of N 1s in CZT-CS-NPs, CZT-CS-SH-NPs, F-CZT-CS-SH-NPs, CTX-CZT-CS-SH-NPs, and F-CTX-CZT-CS-SH-NPs was found to be 1.01 ± 0.60%, 2.91 ± 0.57%, 5.35 ± 0.21%, 5.80 ± 0.73%, and 8.77 ± 1.24%, respectively. The rise in nitrogen atomic percentage of F-CTX-CZT-CS-SH-NPs can be attributed to the considerably higher nitrogen atoms in the folic acid and CTX, hence supporting the presence of both ligands. In contrast, the atomic percentage of S 2p is present in all CS-SH-NPs with a slight decrease in dual-receptor targeted CS-SH-NPs.

Entrapment Efficiency. Table 1 demonstrates that the entrapment efficiency of all CS-NPs has ranged from 65 to 80%, whereas the entrapment efficiency for the formulation with C6 loading has ranged in between 65 to 73%. The entrapment efficiency in the CZT-CS-NPs is higher than that in CZT-CS-NPs ($p \geq 0.05$), F-CZT-CS-SH-NPs ($p < 0.001$), CTX-CZT-CS-SH-NPs ($p < 0.001$), and F-CTX-CZT-CS-SH-NPs ($p < 0.001$). Since the particles were centrifuged at 1000 rpm for 5 min to remove larger particles that were aggregated. After the conjugation, particle size and density may usually increase. Therefore, the NPs recovery is expected to be less as compared to nontargeted CS-NPs. As there may be a loss of the drug entrapped from the discarded larger particles, the entrapment efficiency of dual and single receptor targeted CS-NPs was found to be slightly lesser. The decline in drug entrapment efficiency in receptor-targeted NPs is also apparent in a study conducted by Mehta et al. In this research, the entrapment efficiency of docetaxel in receptor-targeted NPs was somewhat reduced compared to that of nontargeted NPs.[44]

Degree of Conjugation. UV analysis was used to measure the amount of folic acid in F-CZT-CS-SH-NPs and F-CXT-CZT-CS-SH-NPs, which was found to be 69.3 ± 2.5% and 68.6 ± 2.9%, respectively. Furthermore, our findings on the folic acid content of CS NPs are consistent with those reported

https://doi.org/10.1021/acs.biomac.3c00658
Biomacromolecules XXXX, XXX, XXX−XXX

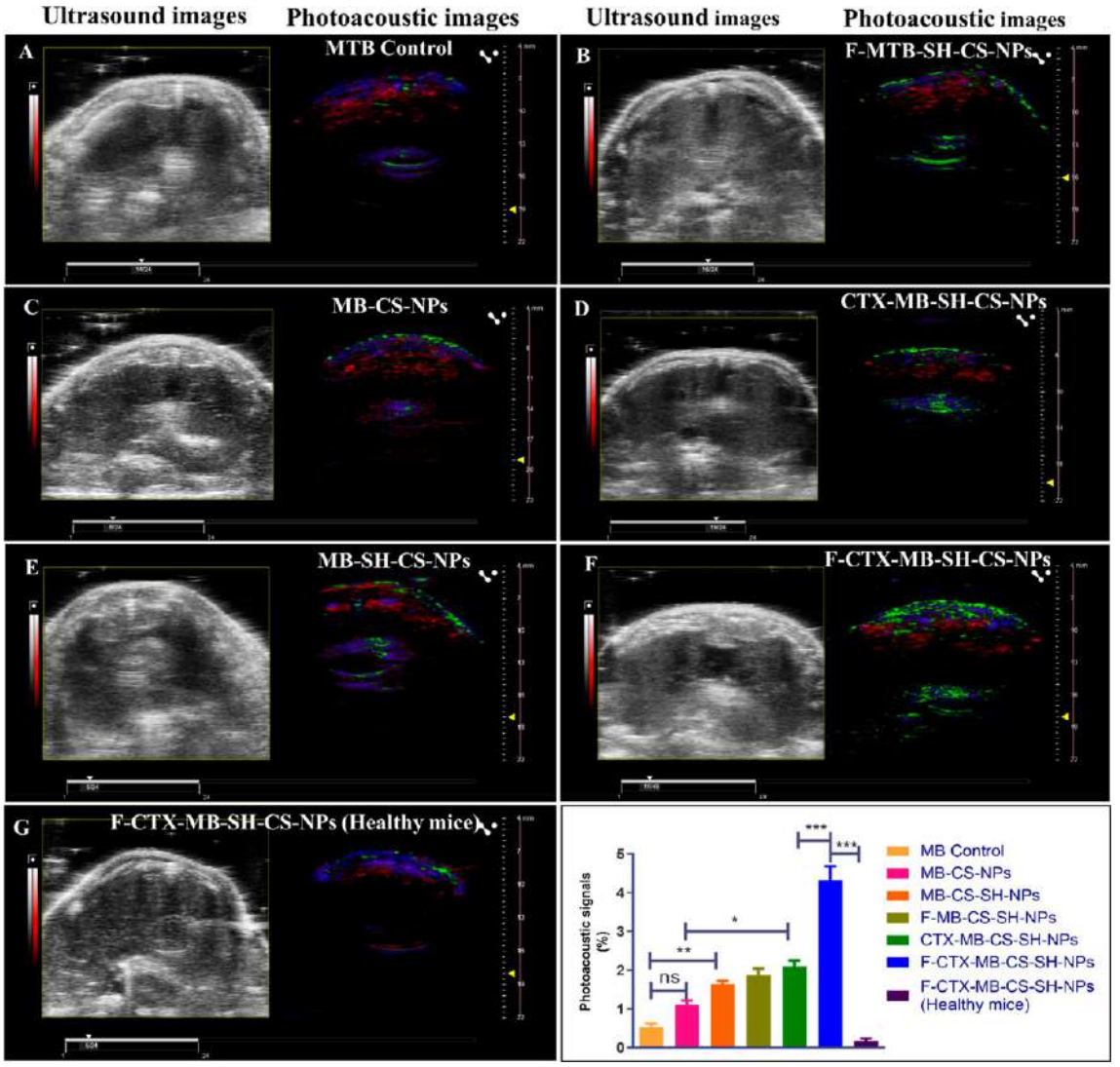

Figure 6. Ultrasound and photoacoustic images of (A to F) the lungs of cancer induced mice after 30 min intravenous injection of MB-control, MB loaded CS-NPs and (G) lung of healthy mice after 30 min intravenous injection of F-CTX-CZT-CS-SH-NPs. (H) Histogram showing the percentage of photoacoustic signals indicating the biodistribution of MB and MB loaded CS-NPs.

by Esfandiarpour et al.[26] In contrast, the Bradford assay revealed that the extent of CTX functionalization on the surfaces of CTX-CZT-CS-SH-NPs and F-CTX-CZT-CS-SH-NPs were 74.37 ± 2.36% and 70.13 ± 3.87%, respectively. The degree of conjugation of folic acid and CTX on dual-receptor targeted NPs was lesser than that of single receptor targeted NPs, which may be due to the interference due to the presence of two ligands. In addition, previous research utilizing both ligands for the delivery of docetaxel also reported a decrease in the degree of folic acid and CTX in dual ligand targeted NPs, which is also consistent with our findings.[15]

X-ray Diffraction (XRD) Analysis. The physical state of nanomedicine can affect the way they interact with cells and tissues in the body, as well as their stability in the bloodstream. Therefore, amorphous and crystalline nanomedicine may differ in terms of efficacy and safety when administered intravenously. Studies have shown that amorphous nanomedicine is more biocompatible for intravenous administration than its crystalline counterparts. The CZT exhibited sharp peaks in XRD (2θ = 15° to 40°), which revealed its crystalline nature (Figure 1B). The drug is, however, adequately loaded in the NPs, as indicated by the fact that the peaks found in the XRD pattern of CZT did not approximate the peaks observed in any of the NPs. The peak pattern of CZT-CS-NPs and CZT-CS-SH-NPs showed broad peaks with several sharp peaks. However, the XRD patterns of F-CZT-CS-SH-NPs, CTX-CZT-CS-SH-NPs, and F-CTX-CZT-CS-SH-NPs were amorphous in nature.

In Vitro Characterization. *In Vitro Drug Release.* The percent release of CZT from various CZT-CS-NPs is shown in Figure 1C, D, E, and F. Initially, the NPs exhibited burst release followed by a sustained release up to 24 h. The release profile of CZT from all the nanoparticles has been examined by calculating the T_{50} value (time required to release 50% of the drug), as shown in Figure S7. The T_{50} value of all SH-NPs was significantly lesser than that of their nonredox-sensitive counterparts, demonstrating their redox-sensitive property as also evident by previous studies.[45,46] Since chitosan is more readily soluble in acidic environments, the chitosan nanoparticles are known for pH-sensitive release.[47] The increased drug release in the cancer microenvironment is supported by the fact that all nanoparticles showed a higher release rate at

https://doi.org/10.1021/acs.biomac.3c00658
Biomacromolecules XXXX, XXX, XXX−XXX

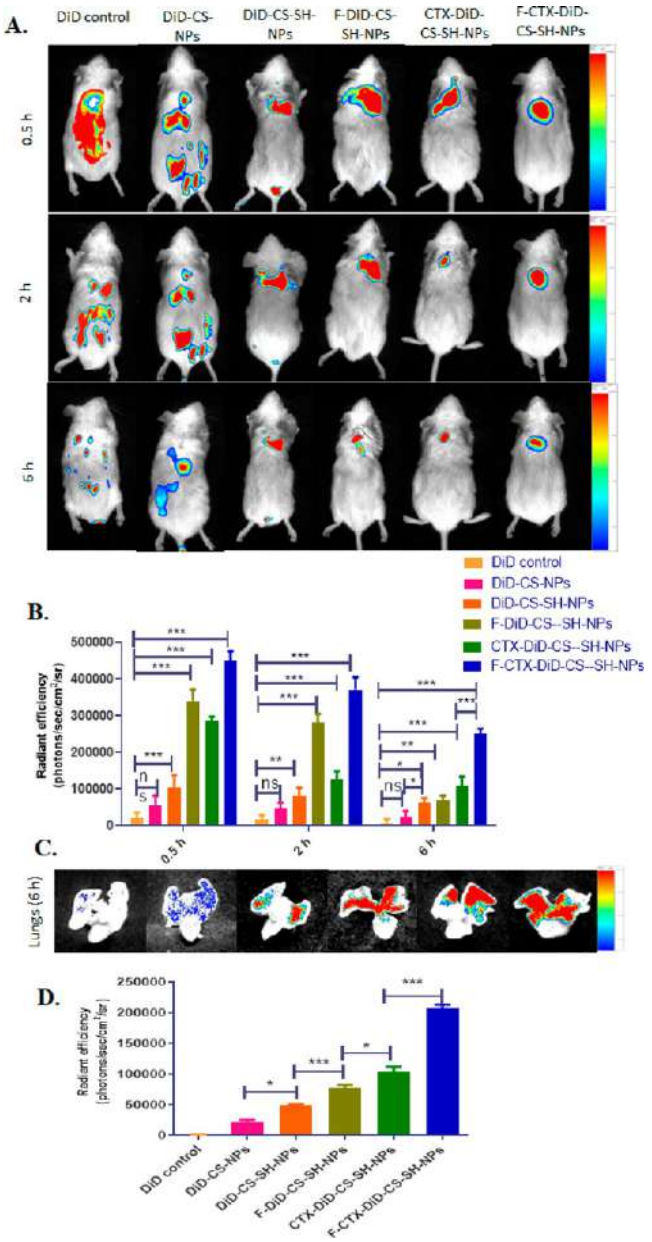

Figure 7. (A) *In vivo* biodistribution of DiD loaded CS-NPs at 0.5, 2, and 6 h after intravenous administration in a B(a)P induced lung cancer model and (B) histogram showing their radiant efficiency. (C) The extracted lungs and heart of animals after 6 h of intravenous administration and (D) histogram showing their radiant efficiency.

pH 5.5 than at pH 7.4. Moreover, the T_{50} of F-CTX-CZT-SH-CS-NPs in GSH media (20 mM) was significantly lower ($p < 0.001$) than that in 5 mM, demonstrating their burst release and confirming their ability to function as redox-sensitive nanoparticles. However, this difference was considerably lesser ($p < 0.05$) when comparing the T_{50} of CZT-CS-NPs with F-CTX-CZT-SH-CS-NPs. The variation in nanoparticle quantity taken for drug release likely contributes to this effect. As the entrapment efficiency of F-CTX-CZT-SH-CS-NPs was lesser than that of CZT-CS-NPs, the higher volume of nanoparticles was required to match CZT concentrations. As a result, differences in the chitosan/CZT ratio in F-CTX-CZT-CS-SH-NPs could have resulted in a insignificant rise in release rate than CZT-CS-NPs.

In Vitro Cellular Uptake Analysis. The green fluorescence images from the fluorescent microscopy of the cells have depicted the internalization of NPs (Figure 3A), which were further quantified using image-J software. The degree of NPs internalization was assessed by image-J software by observing the intensity of green fluorescence. The F-CTX-C6-CS-SH-NPs displayed a percentage of green fluorescence about 107 fold, 3 fold, 2.5 fold, 1.7 fold, and 1.5 fold higher than those of the pure-C6, C6-CS-NPs, C6-CS-SH-NPs, F-C6-CS-SH-NPs, and CTX-C6-CS-SH-NPs ($p < 0.001$; Figure 3B). Moreover, the blue channel images, in the cellular-uptake study, revealed no fragmentation of the nuclei. Therefore, it can be concluded that the cellular uptake occurred in the normal cell morphology. The results demonstrated that the overexpression of folate and EGF receptors promoted the higher uptake of F-CTX-C6-CS-SH-NPs in A549 cells. Moreover, both receptors share an endocytic pathway, which considerably fostered the uptake of targeted CS-NPs (via-caveolae).

MTT Assay. To compare the cytotoxicity of thiolated CS-NPs in A549 cells and SIRC (control cells), a set of nonthiolated CS-NPs was also prepared. The CZT control and all the prepared NPs exhibited dose dependence on cytotoxicity toward A549 cells and SIRC cells (Figure 4A). However, the cytotoxicity of all CS-SH-NPs was considerably higher as compared to their corresponding CS-NPs (nonredox sensitive). The cell viability of F-CTX-CZT-CS-SH-NPs was significantly lower at each concentration than that of the CZT control and all other CS-NPs. The IC_{50} value of CZT-CS-NPs, CZT-CS-SH-NPs, F-CZT-CS-SH-NPs, CTX-CZT-CS-SH-NPs, and F-CTX-CZT-CS-SH-NPs was 15.73 ± 2.3 μg/mL, 9.6 ± 1.52 μg/mL, 6.4 ± 0.85 μg/mL, 2.82 ± 0.66 μg/mL, 1.52 ± 0.37 μg/mL, and 0.26 ± 0.12 μg/mL. MTT assay results showed that the IC_{50} value of F-CTX-CZT-CS-SH-NPs was about 60.5, 36.9, 24.6, 10.76, and 5.8 fold lesser than that of the CZT control, CZT-CS-NPs, CZT-CS-SH-NPs, F-CZT-CS-SH-NPs, and CTX-CS-SH-NPs, respectively (Figure 4B). In SIRC cells, there is no significant difference in cell viability between the CZT control, CZT-CS-NPs, CZT-CS-SH-NPs, F-CZT-CS-SH-NPs, and CTX-CS-SH-NPs at each concentration (Figure 4C). Lung cancer is characterized by a higher expression of folate[48] and EGFR[49] as well as higher GSH levels.[50] The significantly higher cytotoxicity of F-CZT-CS-SH-NPs demonstrated the specificity toward cancer cells, possibly due to receptor-mediated endocytosis by two types of receptors, followed by a redox-sensitive thiolation characteristic that triggers the release of CZT in addition to the beneficial proton-sponge effect of positively charged chitosan.

Morphology Assay. After 12 h of incubation of prepared CS-NPs with A549 cells, the F-CTX-CZT-CS-SH-NPs prompted significant nuclear fragmentation and cytoskeleton damage compared to that of the CZT-control as observed under a fluorescent microscope (Figure 5). In addition to the tubulin blocking activity of the CZT, the synergistic dual receptor-mediated cellular uptake, the redox-sensitive sulfhydryl functionalization, and the bioadhesive characteristics of F-CTX-CZT-CS-SH-NPs have collectively improved their cytotoxicity and significantly altered the morphology of the A549 cells when compared to the CZT control.

In Vivo Evaluation. *Induction of Lung Cancer in Mice.* In this study, the antitumor activity of various prepared CS-NPs were evaluated by measuring the nuclei area in the HE-stained slides of the lungs of respective animal groups (Figure 9). However, after the 14th day of the B(a)P exposure, the

https://doi.org/10.1021/acs.biomac.3c00658
Biomacromolecules XXXX, XXX, XXX−XXX

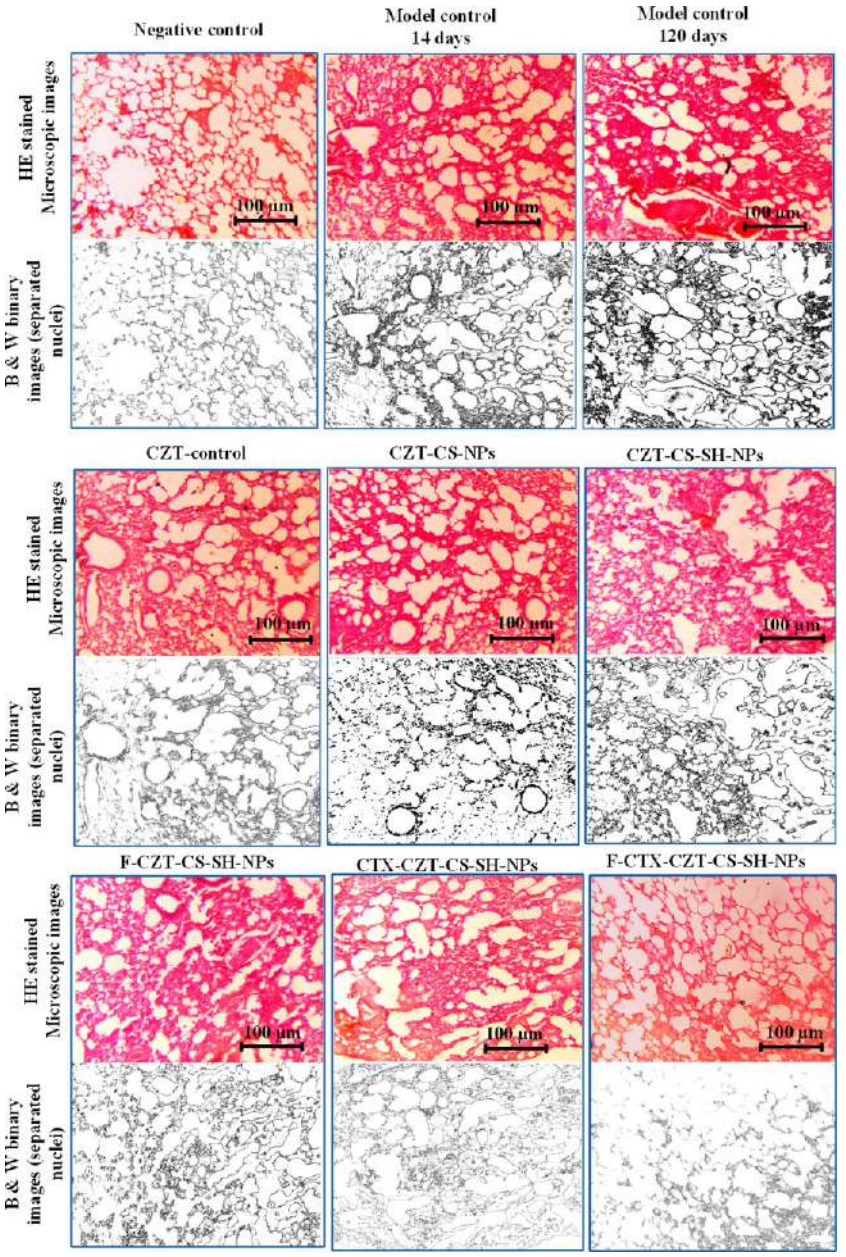

Figure 8. HE stained microscopic and black and white images of separated nuclei of the lungs of animal groups.

histology of the lungs was also examined, and there was a significant increase ($p < 0.05$) in the area of nuclei compared to that of the saline treated animal group, which confirmed the initiation of cancer induction.

Lung Biodistribution by Ultrasound/Photoacoustic Imaging. To support the IVIS live imaging experiment, which represented the targeting ability of the targeted and dual-targeted nanoparticles to lung cancer at 30 min postinjection, the ultrasound/photoacoustic study was also performed at 30 min postinjection of methylene blue loaded CS-NPs (Figure 6A−F). The green photoacoustic signals indicated the presence of the NPs. The percent photoacoustic signals in the lung area of the B(a)P cancer animals treated with the MB control, MB-CS-NPs, MB-CS-SH-NPs, F-MB-CS-SH-NPs, CTX-MB-CS-SH-NPs, and F-CTX-MB-CS-SH-NPs were 0.53 ± 0.15%, 1.12 ± 0.22%, 1.3 ± 0.52%, 1.8 ± 0.31%, 2.11 ± 0.26%, and 4.33 ± 0.61%, respectively. Contrastingly, the percent photoacoustic signals of the healthy mice treated with F-CTX-MB-CS-SH-NPs was 0.17 ± 0.09% (Figure 6G). The percent photoacoustic signals, in the treatment group of F-CTX-MB-CS-SH-NPs, was about 8 fold, 3.8 fold, 2.6 fold, 2.4 fold, and 2 fold higher ($p < 0.001$) as compared to the MB control, MB-CS-NPs, MB-CS-SH-NPs, F-MB-CS-SH-NPs, and CTX-MB-CS-SH-NPs respectively (Figure 6H). Moreover, the photoacoustic signals in the healthy mice treated with F-CTX-MB-CS-SH-NPs were markedly lower (~25 fold; $p < 0.001$), demonstrating its lesser biodistribution in healthy lungs and hence proving its specificity toward cancer. The photoacoustic signals in nontargeted nanoparticles treated cancer-induced mice were significantly higher ($p < 0.001$), when compared with MB control. This demonstrated the EPR effect of nontargeted formulations at the cancer site.

Targeting Efficiency to Lungs by IVIS Live Imaging. The in vivo lung targeting of DiD control and DiD-loaded CS-NPs in B(a)P induced cancer mice was investigated using a real-time fluorescent IVIS imaging system. To compare radiant

https://doi.org/10.1021/acs.biomac.3c00658
Biomacromolecules XXXX, XXX, XXX−XXX

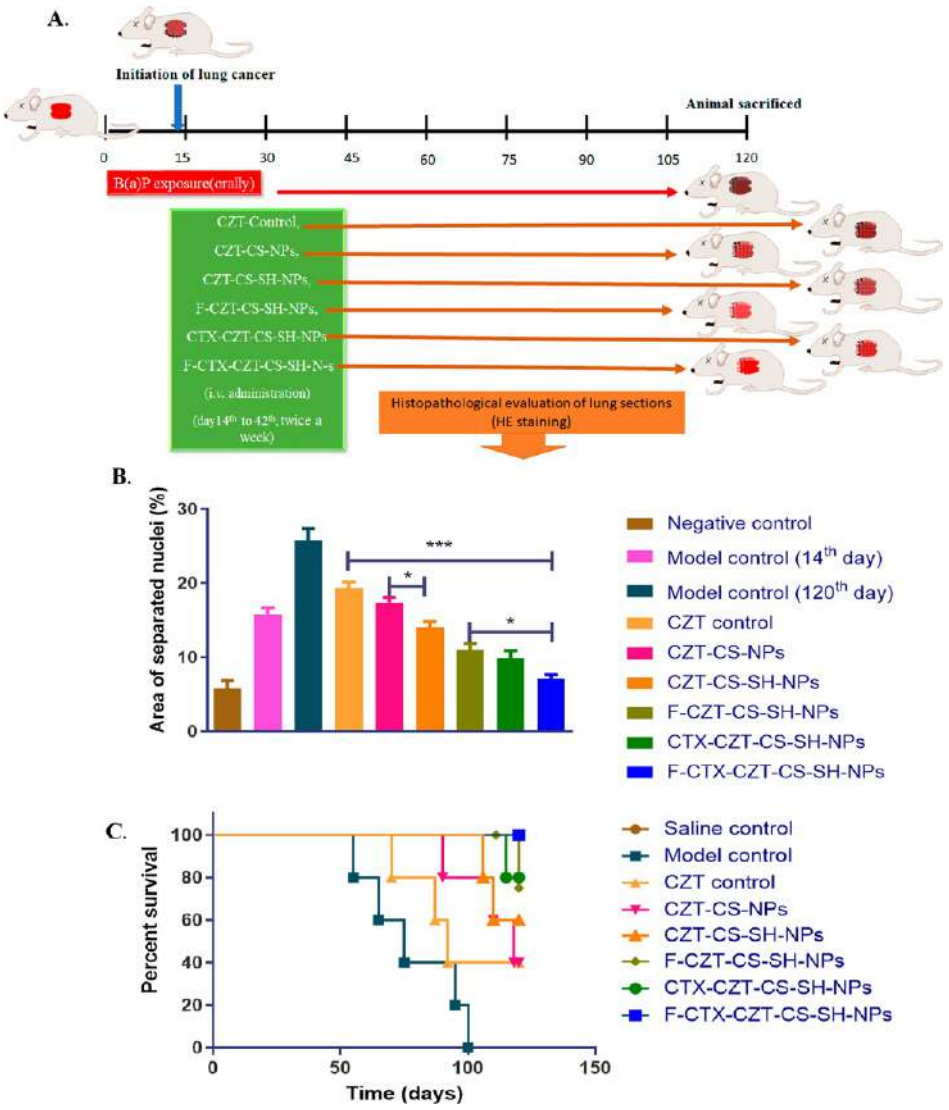

Figure 9. (A) Schematic representation of the cancer induction by B(a)P treatment in Swiss albino mice. (B) Histogram showing the percentage area of separated nuclei from black and white images and (C) showing the percentage survival of the animal after treatment.

efficiency (measured as fluorescence intensity/area/time) for each treatment group at different time points, the Bonferroni two-way analysis was used (Figure 7A,B). The DiD control treated mice at 0.5 h postinjection showed no significant difference in the radiant efficiency compared to that of DiD-CS-NPs, whereas it was significantly higher in the animal groups treated with DiD-CS-SH-NPs ($p < 0.001$), F-DiD-CS-SH-NPs ($p < 0.001$), CTX-DiD-CS-SH-NPs ($p < 0.001$), and F-CTX-DiD-CS-SH-NPs ($p < 0.001$). The DiD control and DiD-CS-NPs showed uneven distribution throughout the mice bodies. After 2 h postinjection, the reduction in radiant efficiency was observed in all treatment groups; however, as compared to mice with DiD control, the DiD-CS-NPs demonstrated no statistically significant differences, whereas it was significantly higher than that of DiD-CS-SH-NPs ($p < 0.01$), F-DiD-CS-SH-NPs ($p < 0.001$), CTX-DiD-CS-SH-NPs ($p < 0.001$), and F-CTX-DiD-CS-SH-NPs ($p < 0.001$). The radiant efficiency in the lung area of DiD control-treated animals after 6 h postinjection showed no significant difference when compared to DiD-CS-NPs, whereas it was significantly higher in DiD-CS-SH-NPs ($p < 0.05$), F-DiD-CS-SH-NPs ($p < 0.01$), CTX-DiD-CS-SH-NPs ($p < 0.001$), and F-CTX-DiD-CS-SH-NPs ($p < 0.001$). The radiant efficiency was significantly higher ($p < 0.05$) in animals treated with DiD-CS-SH-NPs than that of DiD-CS-NPs at 6 h, suggesting superior lung targeting due to their thiolated characteristics. Further, the extracted lungs of the animals treated with DiD control, DiD-CS-NPs, DiD-CS-SH-NPs, F-DiD-CS-SH-NPs, CTX-DiD-CS-SH-NPs, and F-CTX-DiD-CS-SH-NPs after 6 h have shown a radiant efficiency of $(1.13 \pm 0.83) \times 10^3$, $(2.17 \pm 0.61) \times 10^3$, $(4.91 \pm 0.33) \times 10^3$, $(7.72 \pm 0.98) \times 10^3$, $(10.43 \pm 1.36) \times 10^3$, and $(20.66 \pm 1.15) \times 10^3$, respectively (Figure 7C,D). The enhanced radiant efficiency in the lung area of DiD-CS-SH-NPs treated animals could be attributed to their increased mucoadhesion properties due to thiolation as compared to DiD-CS-NPs.[51] The radiant efficiency in the extracted lungs of the animal group at 6 h, treated with F-CTX-DiD-CS-SH-NPs, was about 18.7 fold ($p < 0.0001$), 9.7 fold ($p < 0.0001$), 4.2 fold ($p < 0.0001$), 2.6 fold ($p < 0.001$), and 2 fold ($p < 0.001$) higher as compared to the DiD control, DiD-CS-NPs, DiD-CS-SH-NPs, F-DiD-CS-SH-NPs, and CTX-DiD-CS-SH-NPs, respectively. As a result, the F-CTX-DiD-CS-SH-NPs have achieved effective lung targeting due to improved PEG-assisted circulation times, increased EPR effect,

https://doi.org/10.1021/acs.biomac.3c00658
Biomacromolecules XXXX, XXX, XXX−XXX

dual-receptor targeting, and extended CS and TPGS-SH facilitated bioadhesion followed by endocytosis mediated by folate and EGFR while avoiding accumulation in other organs to minimize the potential side effects.

Survival Analysis and Anticancer Efficacy. Nuclear morphology is one of the most popular and widely used cancer markers because it makes cancer cells easy to distinguish from healthy cells. The main morphologic alterations in malignant cells are nuclear expansion, uneven nuclear outlines, and altered chromatin distribution.[52] Several anticancer treatments can restore normal nuclear structure and function. Advances in understanding nuclear structure provide a platform for the development of new diagnostic tools and therapies.[53] Visualizing excised biopsy specimens stained with HE is considered the gold standard for diagnosing cancer; however, various machine learning techniques are used to diagnose and quantify the extent of malignancy in HE images.[54] In this work, we have quantified the nucleus area in the HE images of the extracted lungs of the treated animal groups as demonstrated by Figure 8. The *in vivo* anticancer efficacy and survival analysis of F-CTX-CZT-CS-SH-NP demonstrated absolute agreement with the results of the *in vitro* cytotoxicity and cellular uptake studies, elucidating its dual-targeting and redox-sensitive release mechanisms. The percentage area of the separated nuclei area of the animal groups treated with saline was 5.8 ± 1.8%, which increase up to 15.5 ± 1.5% ($p < 0.001$) in the animals after the 14th day of B(a)P exposure. The increase in the nuclei area represents the initiation of cancer induction, and therefore, on the same day, the anticancer efficacy study was started by injecting the nanoparticles and CZT control (Figure 9A). However, after the 120th day of B(a)P exposure, the percentage of the nuclei was 25.8 ± 2.7%, which was reduced in the animal treated with the CZT control, CZT-CS-NPs, CZT-CS-SH-NPs, F-CZT-CS-SH-NPs, CTX-CZT-CS-SH-NPs, and F-CTX-CZT-CS-SH-NPs up to 19.3 ± 2.5%, 17.38 ± 1.5%, 14.7 ± 1.3%, 11.3 ± 1.45%, 9.87 ± 1.7%, and 7.1 ± 0.91%, respectively (Figure 9B).

The animal group treated with F-CTX-CZT-CS-SH-NP showed a reduction in the nuclei area of about 3.6 fold in comparison to the cancer model group. Furthermore, the Kaplan−Meier survival analysis also demonstrated that the percent survival rates of lung-cancer-induced mice treated with F-CTX-CZT-CS-SH-NPs ($P < 0.0001$), CTX-CZT-CS-SH-NPs ($P < 0.001$), and F-CZT-CS-SH-NPs ($P < 0.001$) were significantly extended. However, the animal groups treated with CZT control exhibited lesser survival benefits (Figure 9C).

Histopathological Analysis. Histological examination of various vital organs of the saline-treated animals, such as the liver, kidney, lung, and heart, revealed no significant changes in organ architecture (Figure S8). In the CZT control-treated animals, heart fibers were found to be disorganized, and hepatocyte necrosis was widespread. At the same time, histological examination revealed that the animal group treated with CS-NPs only showed partial lesions in the vital organs. The CZT control (marketed injection) is the inclusion of CZT in tween-80 and ethanol and was given saline in solution form; the drug was immediately available to the organs that might have caused the toxicity. Furthermore, tween-80 and ethanol can alter the structure and function of the immune system, resulting in immunotoxicity. However, all redox-sensitive and nonredox-sensitive CS NPs exhibited sustained release of CZT and, therefore, demonstrated reduced organ toxicity. The results from the histopathology study thus affirmed that all prepared CZT-loaded NPs are safer as compared to CZT control (clinical formulation).

CONCLUSION

The present work aims to develop dual-receptor targeted, thiolated CZT nanoparticles for superior anticancer efficacy. The dual receptor-targeted thiolated nanoparticles are hypothesized to be internalized to a higher extent in cancer cells, while chitosan confers the proton-sponge effect and their thiolated mechanism delays lysosomal degradation and activates burst release. As demonstrated by the *in vitro* cellular uptake analysis in A549 cells, the F-CTX-CS-C6-CS-SH-NPs are synergistically uptaken by cancer cells more than nontargeted NPs. Moreover, their *in vitro* release study showed burst release in the GSH-fortified media, simulating the cancer microenvironment. The MTT assay on cancer and non-cancerous cells demonstrated their cancer specificity and endorsed the role of folate and EGF receptors in active targeted delivery followed by the triggered release of CZT due to redox-sensitive thiolated characteristics.

In addition, F-CXT-CZT-CS-SH-NPs also demonstrated potent anticancer efficacy and improved survival in the lung tumor induced mice model compared to other NPs. Further, the thiolated CS-NPs, targeted to the folate receptor and EGFR, demonstrated significantly enhanced lung biodistribution as evident from ultrasound/photoacoustic imaging, which includes MB as a contrasting agent, and better targeting in lungs by IVIS live imaging of NPs loaded with DiD dye as the florescent material on a B(a)P induced lung cancer model. The stealth properties conferred by the PEG of TPGS, the EPR effect due to its small size, and improved bioadhesion by the courtesy of chitosan and sulfhydryl moieties of this futuristic nanosystem are the proposed reasons for the observed benefits. In addition, the histopathology study showed that all CS-NPs proved to be safer in Wistar rats than in the CZT control treated one. The dual receptor targeted, thiolated CS-NPs of CZT were found to be more effective, safer, and specific for cancer than the existing clinical formulations.

ASSOCIATED CONTENT

Supporting Information

The Supporting Information is available free of charge at https://pubs.acs.org/doi/10.1021/acs.biomac.3c00658.

(Text S1) Hydrodynamic size, polydispersity, and surface charge; (Text S2) atomic force microscopy (AFM); (Text S3) transmission electron microscopy (TEM); (Text S4) surface chemistry; (Text S5) degree of conjugation of F and CTX; (Text S6) entrapment efficiency; (Text S7) X-ray diffraction (XRD) analysis, schematic representation for the synthesis of (I) TPGS-COOH and (II) TPGS-SH, FTIR spectra, ^{13}C NMR spectra, HRMS spectra, XPS survey, histogram showing the T50 values, histopathological assessment; (Table S1) FTIR peak assignment; (Table S2) interpretation of the mass (HRMS) spectra; and (Table S3) formulation of various CS-NPs (PDF)

AUTHOR INFORMATION

Corresponding Author

Madaswamy S. Muthu − *Department of Pharmaceutical Engineering and Technology, Varanasi 221005 Uttar*

https://doi.org/10.1021/acs.biomac.3c00658
Biomacromolecules XXXX, XXX, XXX−XXX

Pradesh, India; orcid.org/0000-0001-5805-7921; Phone: +91 9235195928; Email: msmuthu.phe@itbhu.ac.in; Fax: +91 542 2368428

Authors

Vikas − *Department of Pharmaceutical Engineering and Technology, Varanasi 221005 Uttar Pradesh, India*

Abhishesh Kumar Mehata − *Department of Pharmaceutical Engineering and Technology, Varanasi 221005 Uttar Pradesh, India*

Matte Kasi Viswanadh − *Department of Pharmaceutics, College of Pharmacy, K.L. Deemed-to-be-University, Vaddeswaram 522302 Andhra Pradesh, India*

Ankit Kumar Malik − *Department of Pharmaceutical Engineering and Technology, Varanasi 221005 Uttar Pradesh, India*

Aseem Setia − *Department of Pharmaceutical Engineering and Technology, Varanasi 221005 Uttar Pradesh, India*

Pooja Kumari − *School of Biomedical Engineering, Varanasi 221005 Uttar Pradesh, India*

Sanjeev Kumar Mahto − *School of Biomedical Engineering, Varanasi 221005 Uttar Pradesh, India;* orcid.org/0000-0002-5124-545X

Complete contact information is available at: https://pubs.acs.org/10.1021/acs.biomac.3c00658

Notes

The authors declare no competing financial interest.

REFERENCES

(1) Boakye, D.; Günther, K.; Niedermaier, T.; Haug, U.; Ahrens, W.; Nagrani, R. Associations between comorbidities and advanced stage diagnosis of lung, breast, colorectal, and prostate cancer: A systematic review and meta-analysis. *Cancer Epidemiol.* **2021**, *75*, 102054.

(2) Pawlik, T. M.; Devon, K. M.; Fields, C. A.; Hinshaw, D. B. What are patients' expectations about the effects of chemotherapy for advanced cancer? *J. Am. Coll. Surg.* **2014**, *219* (3), 588−590.

(3) Perillo, B.; Di Donato, M.; Pezone, A.; Di Zazzo, E.; Giovannelli, P.; Galasso, G.; Castoria, G.; Migliaccio, A. ROS in cancer therapy: the bright side of the moon. *Exp. Mol. Med.* **2020**, *52* (2), 192−203.

(4) Kennedy, L.; Sandhu, J. K.; Harper, M. E.; Cuperlovic-Culf, M. Role of Glutathione in Cancer: From Mechanisms to Therapies. *Biomolecules* **2020**, *10* (10), 1429.

(5) Tseng, S. H.; Chou, M. Y.; Chu, I. M. Cetuximab-conjugated iron oxide nanoparticles for cancer imaging and therapy. *Int. J. Nanomedicine* **2015**, *10*, 3663−3685.

(6) Bonet-Aleta, J.; Sancho-Albero, M.; Calzada-Funes, J.; Irusta, S.; Martin-Duque, P.; Hueso, J. L.; Santamaria, J. Glutathione-triggered catalytic response of copper-iron mixed oxide nanoparticles. leveraging tumor microenvironment conditions for chemodynamic therapy. *J. Colloid Interface Sci.* **2022**, *617*, 704−717.

(7) Zheng, N.; Song, Z.; Liu, Y.; Zhang, R.; Zhang, R.; Yao, C.; Uckun, F. M.; Yin, L.; Cheng, J. Redox-responsive, reversibly-crosslinked thiolated cationic helical polypeptides for efficient siRNA encapsulation and delivery. *J. Controlled Release* **2015**, *205*, 231−239.

(8) Yang, X.; Cai, X.; Yu, A.; Xi, Y.; Zhai, G. Redox-sensitive self-assembled nanoparticles based on alpha-tocopherol succinate-modified heparin for intracellular delivery of paclitaxel. *J. Colloid Interface Sci.* **2017**, *496*, 311−326.

(9) Sharma, P. K.; Sharma, H. P.; Chakole, C. M.; Pandey, J.; Chauhan, M. K. Application of Vitamin E TPGS in ocular therapeutics - Attributes beyond excipient. *J. Indian Chem. Soc.* **2022**, *99* (3), 100387.

(10) Chen, C. C.; Fa, Y. C.; Kuo, Y. Y.; Liu, Y. C.; Lin, C. Y.; Wang, X. H.; Lu, Y. H.; Chiang, Y. H.; Yang, C. M.; Wu, L. C.; et al. Thiolated mesoporous silica nanoparticles as an immunoadjuvant to enhance efficacy of intravesical chemotherapy for bladder cancer. *Adv. Sci. (Weinh)* **2023**, *10* (7), No. e2204643.

(11) Nayak, J.; Prajapati, K. S.; Kumar, S.; Vashistha, V. K.; Sahoo, S. K.; Kumar, R. Thiolated β-cyclodextrin modified iron oxide nanoparticles for effective targeted cancer therapy. *Mater. Today Commun.* **2022**, *33*, 104644.

(12) Song, X.; Wu, J.; Song, W.; Chen, L.; Zhang, S.; Ji, H.; Liu, J.; Gu, J. Thiolated chitosan nanoparticles for stable delivery and smart release of As_2O_3 for liver cancer through dual actions. *Carbohydr. Polym.* **2023**, *303*, 120462.

(13) Gao, J.; Huang, X.; Liu, H.; Zan, F.; Ren, J. Colloidal stability of gold nanoparticles modified with thiol compounds: bioconjugation and application in cancer cell imaging. *Langmuir* **2012**, *28* (9), 4464−4471.

(14) Jiang, L.; Li, X.; Liu, L.; Zhang, Q. Thiolated chitosan-modified PLA-PCL-TPGS nanoparticles for oral chemotherapy of lung cancer. *Nanoscale Res. Lett.* **2013**, *8* (1), 66.

(15) Vikas; Viswanadh, M. K.; Mehata, A. K.; Sharma, V.; Priya, V.; Varshney, N.; Mahto, S. K.; Muthu, M. S. Bioadhesive chitosan nanoparticles: Dual targeting and pharmacokinetic aspects for advanced lung cancer treatment. *Carbohydr. Polym.* **2021**, *274*, 118617.

(16) Stowers, S. J.; Anderson, M. W. Formation and persistence of benzo(a)pyrene metabolite-DNA adducts. *Environ. Health Perspect.* **1985**, *62*, 31−39.

(17) Duwa, R.; Banstola, A.; Emami, F.; Jeong, J.-H.; Lee, S.; Yook, S. Cetuximab conjugated Temozolomide-loaded poly (lactic-co-glycolic acid) nanoparticles for targeted nanomedicine in EGFR overexpressing cancer cells. *J. Drug Delivery Sci. Technol.* **2020**, *60*, 101928.

(18) Deepagan, V. G.; Sarmento, B.; Menon, D.; Nascimento, A.; Jayasree, A.; Sreeranganathan, M.; Koyakutty, M.; Nair, S. V.; Rangasamy, J. In vitro targeted imaging and delivery of camptothecin using cetuximab-conjugated multifunctional PLGA-ZnS nanoparticles. *Nanomedicine (London, England)* **2012**, *7* (4), 507−519.

(19) Wang, J. K.; Zhou, Y. Y.; Guo, S. J.; Wang, Y. Y.; Nie, C. J.; Wang, H. L.; Wang, J. L.; Zhao, Y.; Li, X. Y.; Chen, X. J. Cetuximab conjugated and doxorubicin loaded silica nanoparticles for tumor-targeting and tumor microenvironment responsive binary drug delivery of liver cancer therapy. *Mater. Sci. Eng., C* **2017**, *76*, 944−950.

(20) Jin, X.; Zhang, J.; Jin, X.; Liu, L.; Tian, X. Folate receptor targeting and cathepsin b-sensitive drug delivery system for selective cancer cell death and imaging. *ACS Med. Chem. Lett.* **2020**, *11* (8), 1514−1520.

(21) Zamboulis, A.; Nanaki, S.; Michailidou, G.; Koumentakou, I.; Lazaridou, M.; Ainali, N. M.; Xanthopoulou, E.; Bikiaris, D. N. Chitosan and its derivatives for ocular delivery formulations: recent advances and developments. *Polymers* **2020**, *12* (7), 1519.

(22) Ibrahim, W. N.; Muizzuddin Bin Mohd Rosli, L.; Doolaanea, A. A. Formulation, cellular uptake and cytotoxicity of thymoquinone-loaded PLGA nanoparticles in malignant melanoma cancer cells. *Int. J. Nanomedicine* **2020**, *15*, 8059−8074.

(23) Moore, C.; Chen, F.; Wang, J.; Jokerst, J. V. Listening for the therapeutic window: Advances in drug delivery utilizing photoacoustic imaging. *Adv. Drug Delivery Rev.* **2019**, *144*, 78−89.

(24) Mandl, H. K.; Quijano, E.; Suh, H. W.; Sparago, E.; Oeck, S.; Grun, M.; Glazer, P. M.; Saltzman, W. M. Optimizing biodegradable nanoparticle size for tissue-specific delivery. *J. Controlled Release* **2019**, *314*, 92−101.

(25) Mansouri, S.; Cuie, Y.; Winnik, F.; Shi, Q.; Lavigne, P.; Benderdour, M.; Beaumont, E.; Fernandes, J. C. Characterization of folate-chitosan-DNA nanoparticles for gene therapy. *Biomaterials* **2006**, *27* (9), 2060−2065.

(26) Esfandiarpour-Boroujeni, S.; Bagheri-Khoulenjani, S.; Mirzadeh, H.; Amanpour, S. Fabrication and study of curcumin loaded nanoparticles based on folate-chitosan for breast cancer therapy application. *Carbohydr. Polym.* **2017**, *168*, 14−21.

(27) Muthu, M. S.; Kutty, R. V.; Luo, Z.; Xie, J.; Feng, S. S. Theranostic vitamin E TPGS micelles of transferrin conjugation for

targeted co-delivery of docetaxel and ultra bright gold nanoclusters. *Biomaterials* **2015**, *39*, 234−248.
(28) Viswanadh, M. K.; Agrawal, N.; Azad, S.; Jha, A.; Poddar, S.; Mahto, S. K.; Muthu, M. S. Novel redox-sensitive thiolated TPGS based nanoparticles for EGFR targeted lung cancer therapy. *Int. J. Pharm.* **2021**, *602*, 120652.
(29) Iyer, R.; Nguyen, T.; Padanilam, D.; Xu, C.; Saha, D.; Nguyen, K. T.; Hong, Y. Glutathione-responsive biodegradable polyurethane nanoparticles for lung cancer treatment. *J. Controlled Release* **2020**, *321*, 363−371.
(30) Cafaggi, S.; Russo, E.; Stefani, R.; Leardi, R.; Caviglioli, G.; Parodi, B.; Bignardi, G.; De Totero, D.; Aiello, C.; Viale, M. Preparation and evaluation of nanoparticles made of chitosan or N-trimethyl chitosan and a cisplatin-alginate complex. *J. Controlled Release* **2007**, *121* (1), 110−123.
(31) dos Santos, T.; Varela, J.; Lynch, I.; Salvati, A.; Dawson, K. A. Effects of transport inhibitors on the cellular uptake of carboxylated polystyrene nanoparticles in different cell lines. *PloS one* **2011**, *6* (9), No. e24438.
(32) Hu, X.; Geetha, R. V.; Surapaneni, K. M.; Veeraraghavan, V. P.; Chinnathambi, A.; Alahmadi, T. A.; Manikandan, V.; Manokaran, K. Lung cancer induced by Benzo(A)Pyrene: ChemoProtective effect of sinapic acid in swiss albino mice. *Saudi J. Biol. Sci.* **2021**, *28* (12), 7125−7133.
(33) Xu, X.; Wu, H.; Yang, Y.; Liu, B.; Tian, J.; Bao, H.; Liu, T. PLGA-coated methylene blue nanoparticles for photoacoustic imaging and photodynamic/photothermal cascaded precisely synergistic therapy of tumor. *RSC Adv.* **2022**, *12* (3), 1543−1549.
(34) Cao, H.; Zhang, Z.; Zhao, S.; He, X.; Yu, H.; Yin, Q.; Zhang, Z.; Gu, W.; Chen, L.; Li, Y. Hydrophobic interaction mediating self-assembled nanoparticles of succinobucol suppress lung metastasis of breast cancer by inhibition of VCAM-1 expression. *J. Controlled Release* **2015**, *205*, 162−171.
(35) Yi, F.; Huang, J.; Yang, L.; Xie, Y.; Xiao, G. Automatic extraction of cell nuclei from H&E-stained histopathological images. *J. Med. Imaging (Bellingham, Wash.)* **2017**, *4* (2), 027502.
(36) Nomier, Y. A.; Alshahrani, S.; Elsabahy, M.; Asaad, G. F.; Hassan, A.; El-Dakroury, W. A. Ameliorative effect of chitosan nanoparticles against carbon tetrachloride-induced nephrotoxicity in Wistar rats. *Pharm. Biol.* **2022**, *60* (1), 2134−2144.
(37) Vikas; Mehata, A. K.; Suseela, M. N. L.; Behera, C.; Kumari, P.; Mahto, S. K.; Muthu, M. S. Chitosan-alginate nanoparticles of cabazitaxel: Design, dual-receptor targeting and efficacy in lung cancer model. *Int. J. Biol. Macromol.* **2022**, *221*, 874−890.
(38) Devendiran, R. M.; Chinnaiyan, S. k.; Yadav, N. K.; Moorthy, G. K.; Ramanathan, G.; Singaravelu, S.; Sivagnanam, U. T.; Perumal, P. T. Green synthesis of folic acid-conjugated gold nanoparticles with pectin as reducing/stabilizing agent for cancer theranostics. *RSC Adv.* **2016**, *6* (35), 29757−29768.
(39) Naglah, A. M.; Refat, M. S.; Al-Omar, M. A.; Bhat, M. A.; AlKahtani, H. M.; Al-Wasidi, A. S. Synthesis of a vanadyl (IV) folate complex for the treatment of diabetes: spectroscopic, structural, and biological characterization. *Drug Des Devel Ther.* **2019**, *13*, 1409−1420.
(40) Girod, M.; Carissan, Y.; Humbel, S.; Charles, L. Tandem mass spectrometry of doubly charged poly(ethylene oxide) oligomers produced by electrospray ionization. *Int. J. Mass Spectrom.* **2008**, *272* (1), 1−11.
(41) Chendo, C.; Charles, L. Generation of doubly charged species from small synthetic polymers in a high pressure MALDI source. *Int. J. Mass Spectrom.* **2017**, *416*, 46−52.
(42) Varray, S.; Aubagnac, J. L.; Lamaty, F.; Lazaro, R.; Martinez, J.; Enjalbal, C. Poly(ethyleneglycol) in electrospray ionization (ESI) mass spectrometry. *Analusis* **2000**, *28*, 263−268.
(43) Subhan, M. A.; Yalamarty, S. S.; Filipczak, N.; Parveen, F.; Torchilin, V. P. Recent advances in tumor targeting via EPR effect for cancer treatment. *Pers. Med.* **2021**, *11*, 571.
(44) Mehata, A. K.; Bharti, S.; Singh, P.; Viswanadh, M. K.; Kumari, L.; Agrawal, P.; Singh, S.; Koch, B.; Muthu, M. S. Trastuzumab decorated TPGS-g-chitosan nanoparticles for targeted breast cancer therapy. *Colloids Surf. B Biointerfaces* **2019**, *173*, 366−377.
(45) Viswanadh, M. K.; Vikas; Jha, A.; Reddy Adena, S. K.; Mehata, A. K.; Priya, V.; Neogi, K.; Poddar, S.; Mahto, S. K.; Muthu, M. S Formulation and in vivo efficacy study of cetuximab decorated targeted bioadhesive nanomedicine for non-small-cell lung cancer therapy. *Nanomedicine* **2020**, *15* (24), 2345−2367.
(46) Wei, X.; Liao, J.; Davoudi, Z.; Zheng, H.; Chen, J.; Li, D.; Xiong, X.; Yin, Y.; Yu, X.; Xiong, J.; et al. Folate receptor-targeted and GSH-responsive carboxymethyl chitosan nanoparticles containing covalently entrapped 6-mercaptopurine for enhanced intracellular drug delivery in leukemia. *Mar Drugs* **2018**, *16* (11), 439.
(47) Mohammed, M. A.; Syeda, J. T. M.; Wasan, K. M.; Wasan, E. K. An Overview of chitosan nanoparticles and its application in non-parenteral drug delivery. *Pharmaceutics* **2017**, *9* (4), 53.
(48) Nunez, M. I.; Behrens, C.; Woods, D. M.; Lin, H.; Suraokar, M.; Kadara, H.; Hofstetter, W.; Kalhor, N.; Lee, J. J.; Franklin, W.; et al. High expression of folate receptor alpha in lung cancer correlates with adenocarcinoma histology and EGFR [corrected] mutation. *J. Thorac Oncol* **2012**, *7* (5), 833−840.
(49) Bethune, G.; Bethune, D.; Ridgway, N.; Xu, Z. Epidermal growth factor receptor (EGFR) in lung cancer: an overview and update. *J. Thoracic Disease* **2010**, *2* (1), 48−51.
(50) Blair, S. L.; Heerdt, P.; Sachar, S.; Abolhoda, A.; Hochwald, S.; Cheng, H.; Burt, M. Glutathione metabolism in patients with non-small cell lung cancers. *Cancer Res.* **1997**, *57* (1), 152−155.
(51) Xu, X.; Liu, K.; Jiao, B.; Luo, K.; Ren, J.; Zhang, G.; Yu, Q.; Gan, Z. Mucoadhesive nanoparticles based on ROS activated gambogic acid prodrug for safe and efficient intravesical instillation chemotherapy of bladder cancer. *J. Controlled Release* **2020**, *324*, 493−504.
(52) Nickerson, J. A. Nuclear dreams: the malignant alteration of nuclear architecture. *J. Cellular Biochemistry* **1998**, *70* (2), 172−180.
(53) Zink, D.; Fischer, A. H.; Nickerson, J. A. Nuclear structure in cancer cells. *Nat. Rev. Cancer* **2004**, *4* (9), 677−687.
(54) Rana, A.; Lowe, A.; Lithgow, M.; Horback, K.; Janovitz, T.; Da Silva, A.; Tsai, H.; Shanmugam, V.; Bayat, A.; Shah, P. Use of deep learning to develop and analyze computational hematoxylin and eosin staining of prostate core biopsy images for tumor diagnosis. *JAMA Netw. Open* **2020**, *3* (5), No. e205111.

https://doi.org/10.1021/acs.biomac.3c00658
Biomacromolecules XXXX, XXX, XXX−XXX